Applied Surface Science 612 (2023) 155892

Contents lists available at ScienceDirect

Applied Surface Science

journal homepage: www.elsevier.com/locate/apsusc

Full Length Article

A novel three-dimensional ordered mesoporous microspheres comprising N-doped graphitic carbon-coated Fe_xP nanoparticles as multifunctional interlayers to suppress polysulfide crossover in Li–S batteries

Rakesh Saroha, Hye Seon Ka, Jung Sang Cho *

Department of Engineering Chemistry, Chungbuk National University, Chungbuk 361-763, Republic of Korea

ARTICLE INFO

Keywords:
Three-dimensional ordered mesopores microspheres
N-doped graphitic carbon
Polar material
Multifunctional interlayer
Li–S batteries

ABSTRACT

Highly porous and conductive microspheres comprising three-dimensionally ordered arrays of mesopores and biphasic iron phosphide (Fe_xP) nanoparticles embedded into nitrogen-doped graphitic carbon (NGC) framework (P-Fe_xP@NGC) were synthesized by spray pyrolysis method followed by phosphidation. The ordered arrays of mesopores ($\phi = 40$ nm) were generated *via* the thermal breakdown of the polystyrene nanobeads ($\phi = 100$ nm). The porous structure not only reduces the effective diffusion length for the charged species but also guarantees efficient electrode wetting along with the accommodation of undesired volume perturbations. The highly conductive NGC framework provides numerous conductive paths for rapid electron transfer, which facilitates kinetically favored redox reactions. Additionally, the polar biphasic Fe_xP nanoparticles allow chemical confinement and catalytic conversion of trapped polysulfides, thus enhancing active material utilization. Correspondingly, the assembled Li–S cells featuring the P-Fe_xP@NGC-coated separator exhibit good rate performance (350 mA h g^{-1} at 2.0C) and extended cycling stability at 0.1, 0.5, and 1.0C mainly due to high diffusion of charged species (diffusion coefficient (D_{Li+}) = 10^{-7} cm^2 s^{-1}) and low charge transfer resistance. Even at high sulfur loading (3.46 mg cm^{-2}) and a low electrolyte/sulfur ratio of 5.6 μL mg^{-1}, the Li–S cells exhibit stable cycling performance.

1. Introduction

The Lithium–sulfur (Li–S) battery technology have engrossed significant attention worldwide in the last two and half decades mainly due to high discharge capacity (1675 mA h g^{-1}), which is almost an order of magnitude higher than that of the Li-ion batteries (LIBs) using conventional cathodes ($LiCoO_2$ and $LiFePO_4$) [1–6]. Additionally, high volumetric (2800 Wh L^{-1}) and gravimetric (2500 Wh kg^{-1}) energy densities, cost-effectiveness owing to S abundance, and low toxicity make Li–S batteries a viable alternative to LIBs [6–10]. However, Li–S batteries encounter various intrinsic problems, such as the low electrical conductivity of elemental S (~10^{-30} S cm^{-1} at ambient conditions), well-known parasitic "shuttle-effect" of highly soluble high-order lithium polysulfide (LiPS) species, i.e., Li_2S_x; $x = 4$, 6, and 8, considerable volume changes during electrochemical redox reactions (~80 %), and poor Li anode stability [11–20]. The low conductivity leads to slow reaction kinetics and charge transfer, whereas large volume changes cause pulverization of the electrode material during repeated cycling [7]. Similarly, uncontrolled LiPS diffusion results in continuous charging processes that can cause short-circuiting of the cell. In addition, the constant loss of active electrode material due to polysulfide migration is responsible for the overall inferior electrochemical performance of Li–S cells in terms of poor reaction kinetics, low Coulombic efficiency, rapid capacity fading, poor rate capability, unstable cycling performance, and corrosion of Li-metal anodes [21]. These drawbacks hinder the feasibility of Li–S batteries.

To surmount these shortcomings, tremendous progress has been made, including the physical confinement of elemental S inside the highly conductive and porous carbon matrices [22–24], chemical confinement of LiPS species using various polar materials [25–27], electrolyte additives [28–30], and protection of the Li anode [31–33]. In this regard, the use of additional interlayer components (free-standing or separator-coated) inside the cell is another strategy that has gained considerable importance because of its ease of application. The interlayer not only acts as a second current collector but also plays a multifunctional role that includes polysulfide confinement, absorbing

* Corresponding author.
E-mail address: jscho@cbnu.ac.kr (J.S. Cho).

https://doi.org/10.1016/j.apsusc.2022.155892
Received 8 October 2022; Received in revised form 24 November 2022; Accepted 26 November 2022
Available online 29 November 2022

unwanted volume variations, and allowing rapid charge diffusion processes. Therefore, to satisfy the above requirements, the interlayer material should be porous enough to accommodate the volume fluctuations along with efficient electrolyte penetration and must have a polar material that provides enough active chemisorption sites for polysulfide anchoring.

With respect to porosity, different types of porous nanostructured materials that require multistep synthesis and complicated template removal (hard and soft) procedures have been explored for Li–S batteries [34–41]. For instance, Kim et al. reported the fabrication of a bimodal carbon foam with a discharge capacity of 420 mA h g^{-1} at 2.0C-rate using a multistep synthesis approach [42]. Similarly, Javed et al. adopted a template method to synthesize N and S co-doped microporous 2D carbon nanosheets with a discharge capacity of 730 mA h g^{-1} after 150 continuous cycles [43]. However, the facile synthesis and applicability of three-dimensionally ordered mesoporous (3-DOM) microspheres embedded in a highly conductive nitrogen-doped graphitic carbon (NGC) framework have not been presented till date for Li–S batteries. The presence of polar material is another much-sought parameter for an ideal interlayer material. Previous studies explored various metal-based polar materials for chemisorption of polysulfide molecules, including metals [44], metal nitrides [11,45,46], metal oxides [8,47–49], metal sulfides [50–52], metal selenides [53–55], and others [56–58]. Transition metal phosphides are of particular interest because of their higher electrical conductivity than metal oxides or sulfides [59,60]. Additionally, their high thermal stability and low charge–discharge voltages make them ideal candidates for use in Li–S batteries [61].

Based on the above discussion, we investigate the morphological and electrochemical performance of highly porous three-dimensional (3D) microspheres with ordered arrays of mesopores and biphasic iron phosphide nanoparticles (Fe_xP) well-embedded inside highly conductive NGC skeleton (hereafter referred to as "P-Fe_xP@NGC") as a multifunctional interlayer in Li–S batteries. The 3D nanostructure was obtained using a scalable spray pyrolysis technique, whereas ordered mesopores were formed by the thermal decomposition of size-controlled polystyrene (PS) nanobeads. The porous structure guarantees an efficient electrolyte penetration and diminishes unsought volume fluctuations during electrochemical testing. The highly conductive NGC framework not only boosts the overall electronic conductivity of nanostructure but also provides enormous conductive pathways for fast charge transfer to allow rapid redox kinetics. Moreover, the biphasic Fe_xP nanoparticles act as chemisorption sites for efficient anchoring and electrocatalytic transformation of polysulfide molecules. Correspondingly, the as-prepared P-Fe_xP@NGC microspheres were applied as a functional coating on a polypropylene separator and used as an interlayer on the cathode side. Employing the proposed P-Fe_xP@NGC multifunctional interlayer, we showed that Li–S cells display improved electrochemical properties in terms of rate capability, cycling stability, and Li-ion diffusion. Overall, we believe that the detailed analysis of physical and electrochemical properties presented here will provide remarkable insights into the development of highly conductive and porous nanostructures as multifunctional interlayers for rechargeable battery applications.

2. Preparation of P-Fe_xP@NGC microspheres

The 3D ordered mesoporous P-Fe_xP@NGC microspheres were synthesized using a facile and scalable spray pyrolysis method, followed by phosphidation. Briefly, 24.6 g of $Fe(NO_3)_3{\cdot}9H_2O$ (KANTO CHEMICAL Co. Inc., 98.5 %, molecular weight (M_w) = 404) and 4.0 g of polyvinylpyrrolidone (PVP) (DAEJUNG, M_w = 40000) were dissolved in 200 mL of deionized (DI) water followed by the addition of a colloidal suspension of PS nanobeads (ϕ = 100 nm, V = 200 mL) and stirred vigorously overnight under ambient conditions. The PS nanobeads act as pore-generating agents and were synthesized using a polymerization technique reported before [62]. The final spray solution was then moved to an ultrasonic atomizer unit attached to a vertically placed preheated quartz tube. The droplets formed by the ultrasonic nebulizer were passed through the quartz tube heated to 700 °C in an N_2 atmosphere at a flow rate of 10 L min^{-1}. The as-sprayed powders were exposed to two-step heat treatment at a heating rate of 5 °C min^{-1}. During the first heating step, the as-sprayed powders were heated at 600 °C for 3 h in a reductive atmosphere (5 % H_2/Ar). Subsequently, during phosphidation, the reduced powders were exposed to the PH_3 gas at 600 °C for 3 h in an identical environment. For this, H_2NaO_2P (Sigma-Aldrich, 98 %, M_w = 87.98) was used as a phosphorus precursor to produce PH_3 gas, and the mass ratio of H_2NaO_2P to the active material was set at 1:5. The obtained final powder was denoted as P-Fe_xP@NGC. A control sample without Fe_xP phase (denoted as "P-NGC" microspheres) was also obtained from the above-mentioned reduced powder *via* an etching process using hydrochloric acid. The material characterization, cell fabrication, and polysulfide adsorption test details are provided in the supporting file.

3. Results and discussion

3.1. Characterization of the synthesized powders

The detailed synthesis procedure of three-dimensional ordered mesoporous microspheres comprising biphasic iron phosphide nanoparticles grafted in N-doped graphitic carbon matrix (P-Fe_xP@NGC) *via* a highly feasible spray pyrolysis method, followed by successive heat treatments, is presented in Scheme 1. The spherical droplets produced by the atomizer consisted of a homogeneous aqueous dispersion of Fe salt, PVP, and PS nanobeads (ϕ = 100 nm), as shown in Scheme 1a-①. Subsequently, the droplets were allowed to pass through a vertically aligned quartz reactor preheated to 700 °C using N_2 as the carrier gas. This step resulted in the formation of iron oxide from the iron nitrate precursor and thermal decomposition of PS nanobeads, thus generating uniformly distributed mesopores throughout the microspheres. In addition, PVP was transformed into amorphous carbonaceous species, which restricted the agglomeration and grain growth of iron oxide nanoparticles. This resulted in the synthesis of 3-DOM nanostructures comprising uniformly distributed Fe_2O_3 nanoparticles inside a carbon matrix (C-matrix), as shown in Scheme 1a-②. Notably, the direct phosphidation of the as-sprayed powders was hindered by the presence of a thick layer of the C-matrix surrounding the Fe_2O_3 nanocrystals, which did not allow the penetration of the phosphine gas (Scheme 1b-①). This issue was overcome by an additional heat treatment step at 600 °C in a reductive atmosphere (5 % H_2/Ar), which not only caused the phase change of Fe_2O_3 nanoparticles to metallic Fe nanocrystals but also allowed efficient conversion of the thick C layers to a more uniform and thin NGC layer due to the catalytic effect of the metallic Fe (Scheme 1a-③). This reduction step is believed to introduce defects that allow facile diffusion and interaction of the PH_3 gas with the metallic Fe nanocrystals during the subsequent phosphidation (Scheme 1b-②). During the final heat treatment process for phosphidation at 600 ℃, the metallic-Fe nanocrystals converted to the biphasic Fe_xP nanoparticles well-embedded inside the NGC matrix. Correspondingly, a three-dimensional ordered mesoporous nanostructure comprising Fe_xP nanoparticles in the NGC-matrix (abbreviated as "P-Fe_xP@NGC" microspheres) was successfully synthesized (Scheme 1a-④). Similarly, 3-DOM microspheres without Fe_xP nanoparticles (P-NGC microspheres) were also synthesized *via* acid etching (metallic Fe etching) of the reduced powder (Scheme 1a-③).

The formation mechanism of the P-Fe_xP@NGC microspheres was investigated by systematic microstructural characterizations of the powders obtained after each synthesis step. The results of the morphological and phase analyses of the 3-DOM microspheres obtained after spray pyrolysis are presented in Fig. 1. FE-SEM micrographs in Fig. 1a suggest the formation of spherical non-aggregated microspheres with an

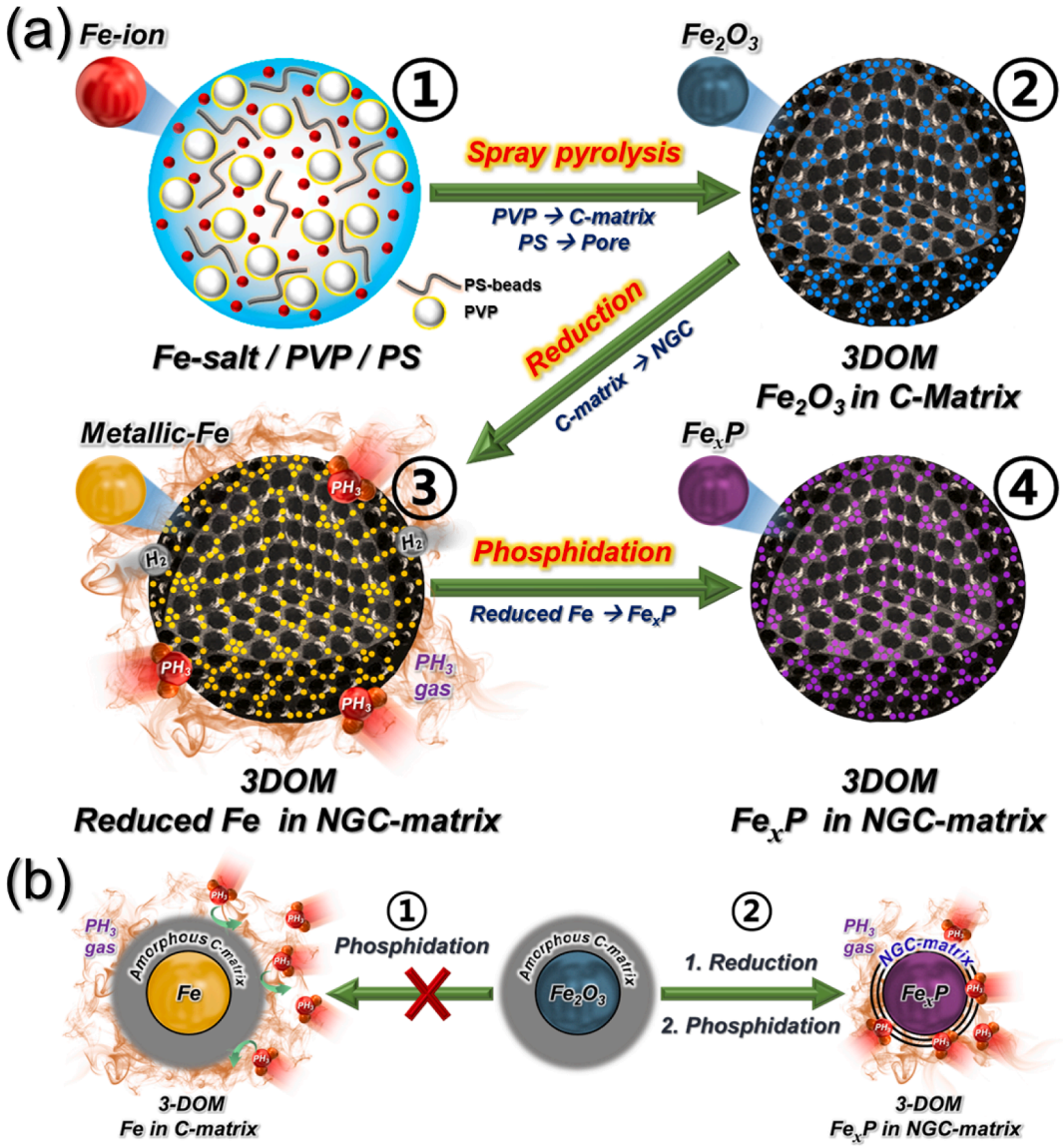

Scheme 1. (a) Schematic representation (Scheme 1a-①-④) of the formation mechanism of 3-DOM Fe_xP@NGC microspheres (P-Fe_xP@NGC) using spray pyrolysis technique and (b) conversion mechanism of Fe_2O_3 to Fe_xP *via* an intermediate reduction step followed by phosphidation process.

average diameter of 1.0 μm. Additionally, the high-magnification FE-SEM image in Fig. 1b indicates the presence of evenly distributed ordered arrays of mesopores on the microsphere surface. The high-magnification FE-SEM micrograph in Fig. 1c exhibits mesopores with a mean diameter of ~ 45 nm, formed owing to the thermal breakdown of the PS nanobeads during the spray pyrolysis. Notably, the pore diameter decreases from 100 nm to 45 nm primarily due to the shrinkage of the microspheres during the spray pyrolysis process. The XRD profile of as-sprayed powder in Fig. 1d show sharp and narrow peaks that were ascribed to crystalline Fe_2O_3.

The as-sprayed 3-DOM powders were subjected to additional heating in a reducing atmosphere (5 % H_2/Ar) before phosphidation. As discussed above, this additional heating step immediately after spraying was needed because of the ineffective phosphidation of as-sprayed powders due to the presence of a thick amorphous carbon matrix surrounding the Fe_2O_3 nanocrystals. To verify this hypothesis, XRD measurements were performed for the as-sprayed powders that were heated at 600 °C under a reductive atmosphere in the presence of a phosphorous salt (H_2NaO_2P). The corresponding XRD profile in Fig. S1 shows distinct diffraction peaks that were designated to the metallic Fe only. Accordingly, an intermediate heating step in a reduction atmosphere was applied and the morphological and crystal structure results are presented in Fig. S2. FE-SEM analysis (Fig. S2a) reveals that the original morphology of the microspheres with a mean diameter of 0.9 μm and ordered arrays of mesopores that were evenly distributed over the surface of the microspheres remained intact (Fig. S2a and 2b). Besides, it was observed that the size of mesopores shrinks a bit (~38 nm) compared to 45 nm for as-sprayed powder. This is due to the removal of the amorphous carbon matrix that alleviates the crystallization and grain growth of Fe-nanocrystals during the phase conversion process, as evident from the high-magnified FE-SEM micrograph in Fig. S2c. The clear presence of Fe-nanocrystals is highly apparent compared to the Fe_2O_3 nanocrystals in Fig. 1c. The XRD pattern, shown in Fig. S2d, also confirms the formation of a metallic Fe phase during the reduction process. Therefore, the reduction step ensures the formation of 3-DOM microspheres comprising metallic Fe nanocrystals embedded in the NGC matrix.

The 3-DOM reduced powders obtained above were further utilized for a phosphidation process under a reductive atmosphere (5 % H_2/Ar). The process was performed at 600 °C for 3 h whereas H_2NaO_2P salt was used as a phosphorus precursor. The microstructural and phase characteristics of P-Fe_xP@NGC microspheres obtained after phosphidation

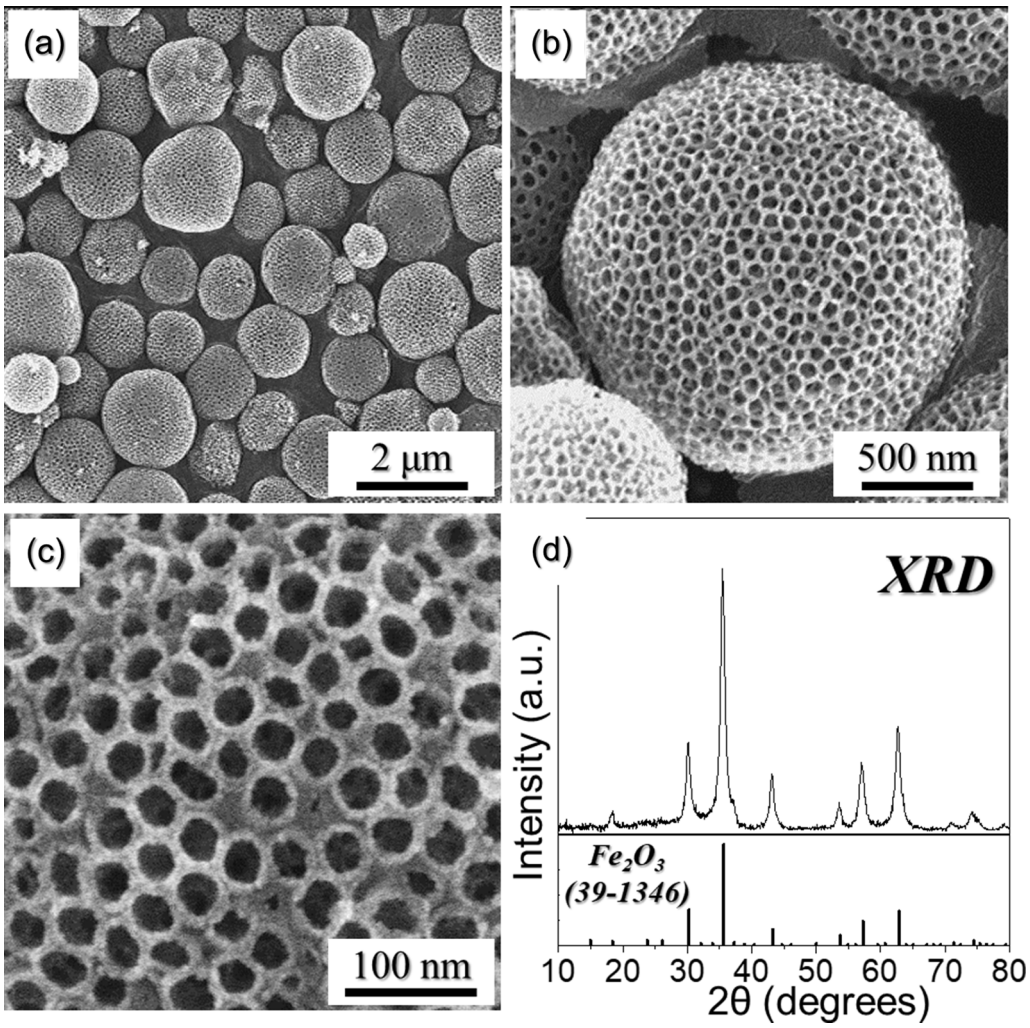

Fig. 1. Physical characterizations of the as-sprayed microspheres obtained after spray pyrolysis at 700 ℃: (a,b) low-magnification FE-SEM images, (c) high magnification FE-SEM image, and (d) XRD pattern.

are presented in Fig. 2. FE-SEM micrograph in Fig. 2a shows microsphere morphology (mean diameter = 0.8 μm). Besides, no agglomeration or structural deformation, such as fracturing or rupturing, was observed, suggesting high structural integrity of the microspheres. The FE-SEM image at high magnification in Fig. 2b implies that ordered arrays of mesopores are still present in the microspheres. Moreover, the crystallization and grain growth of the metallic-Fe nanocrystals resulted in the formation of biphasic Fe_xP (containing FeP and Fe_2P) nanoparticles, as evident from the high-magnified FE-SEM image in Fig. 2c. The TEM images shown in Fig. 2d and e are consistent with the FE-SEM results, confirming the formation of well dispersed microspheres (average diameter = 0.8 μm). The amplified TEM image in Fig. 2f reveals that the Fe_xP nanoparticles (black region) were incorporated into the NGC framework (gray region). The NGC skeleton was formed from the amorphous carbon matrix during the intermediate reduction process under a reducing atmosphere owing to the catalytic effect of the metallic-Fe nanocrystals. Further, to validate this, a Raman spectrum was obtained for the P-Fe_xP@NGC microspheres, as shown in Fig. S3a. The intensity ratio of D- and G-bands (i.e., I_D/I_G) generally determines the crystallinity of carbonaceous materials [63]. The I_D/I_G ratio for the P-Fe_xP@NGC microspheres was ~ 0.92, indicating that the powders primarily consisted of graphitic carbon. The NGC framework enhances the overall electrical conductivity of the nanostructure, resulting in fast electron transfer through numerous conductive pathways. The increase in conductivity is ascribed to the large electronegative character of the N atom than that of C atom [64–66]. The HR-TEM image in Fig. 2g confirms that NGC layer with a thickness of ~ 3 nm enveloped the Fe_xP nanoparticles. In addition, lattice fringes show d-spacing values of 0.25 and 0.24 nm, that attributed to the (2 0 0) and (1 1 1) planes of Fe_2P and FeP, respectively. The selected area electron diffraction (SAED) and XRD patterns presented in Fig. 2h and i, respectively, are synchronized with the HR-TEM results confirming the presence of the Fe_2P and FeP phases. Notably, the XRD peaks attributed to the Fe_2P phase were more intense than those of the FeP phase. This observation was further confirmed by structural Rietveld refinement technique, which quantifies the proportion of Fe_2P phase as 94.3 % followed by FeP (3.9 %), and graphitic carbon (1.8 %). The goodness of the fitting factor i.e. χ^2 is around 7.02 % which demonstrates that the results are reliable (Fig. S4). The elemental mapping images in Fig. 2j exhibit uniform dispersion of Fe, P, C, and N throughout the P-Fe_xP@NGC microspheres, suggesting the synthesis of a phase-pure material. Overall, the crystal structure and morphological analysis results suggest the successful synthesis of 3-DOM microspheres that comprise biphasic iron phosphide nanoparticles well-embedded in the NGC matrix.

The surface bonding state of different elements in the P-Fe_xP@NGC microspheres was also evaluated using XPS. The survey spectrum in Fig. S5 shows the presence of Fe 2p, O 1 s, N 1 s, C 1 s, P 1 s, and P 2p photoelectron peaks. The Fe 2p core-level XPS spectrum in Fig. 3a exhibits well-fitted peaks attributed to the Fe $2p_{3/2}$ (710.6 eV) and Fe $2p_{1/2}$ (724.7 eV) electronic levels, which matches well with previously

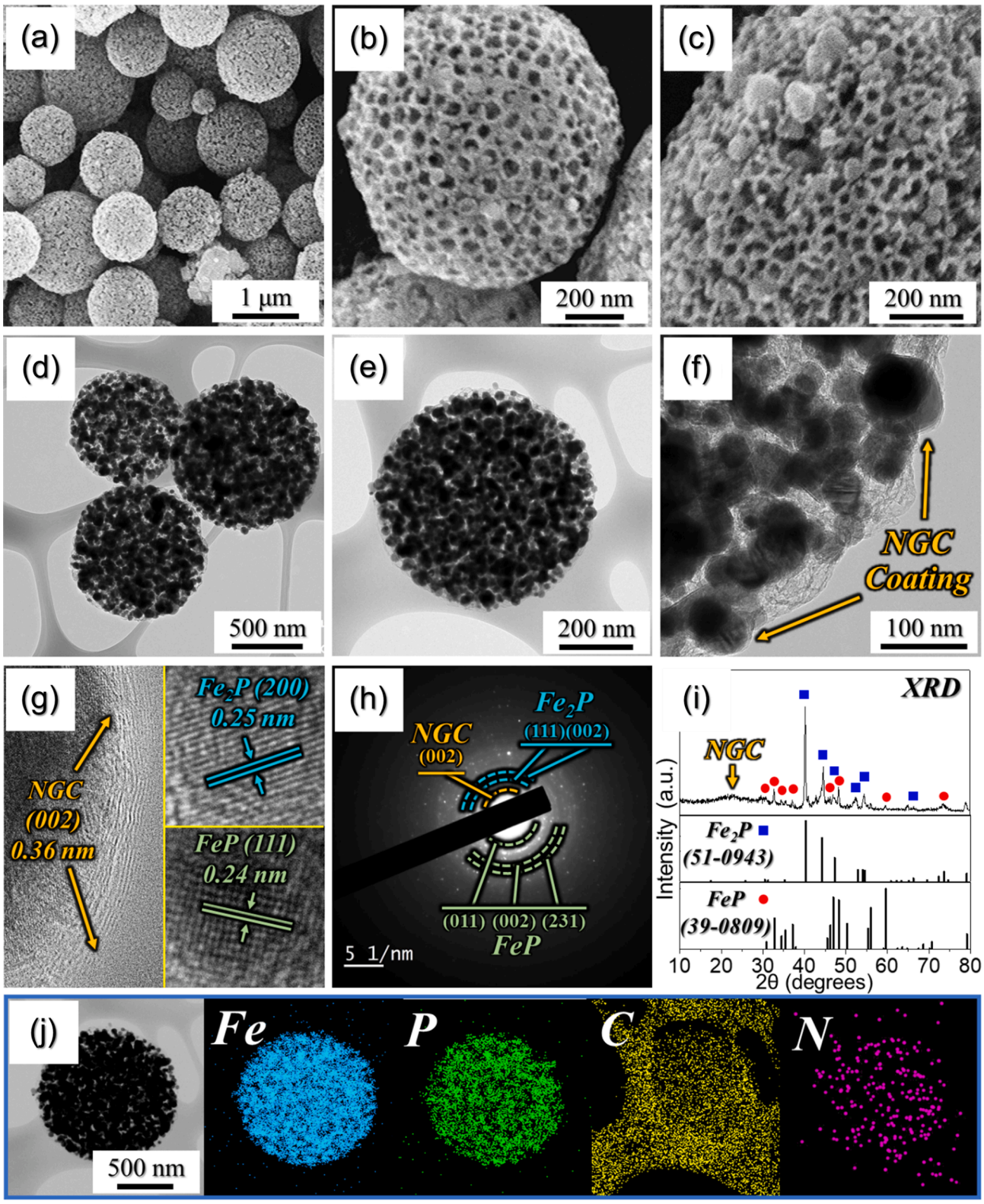

Fig. 2. Characterizations of the P-Fe$_x$P@NGC microspheres obtained after the phosphidation process: (a,b) FE-SEM images, (c) high magnification FE-SEM image, (d-f) TEM images, (g) HR-TEM image, (h) SAED pattern, (i) XRD pattern, and (j) elemental mapping images.

reported values [67,68]. In addition, the Fe 2p spectrum confirms the coexistence of Fe^{2+} and Fe^{3+} oxidation states along with the satellite peak [69]. Moreover, it should be noted that the deconvoluted profile of Fe^{3+} component of Fe $2p_{1/2}$ core level exhibits two fitted peaks. The peak centered at 724.7 eV represents the signature peak of Fe $2p_{1/2}$ core level whereas the deconvoluted peak centered at 723.3 eV is surface peak related to the oxidation of Fe$_x$P nanoparticles and matches well with the previous report [70]. The deconvoluted P 2p core-level XPS spectrum in Fig. 3b shows one predominant peak at 133.4 eV that corresponds to the partial surface oxidation of Fe$_x$P nanoparticles

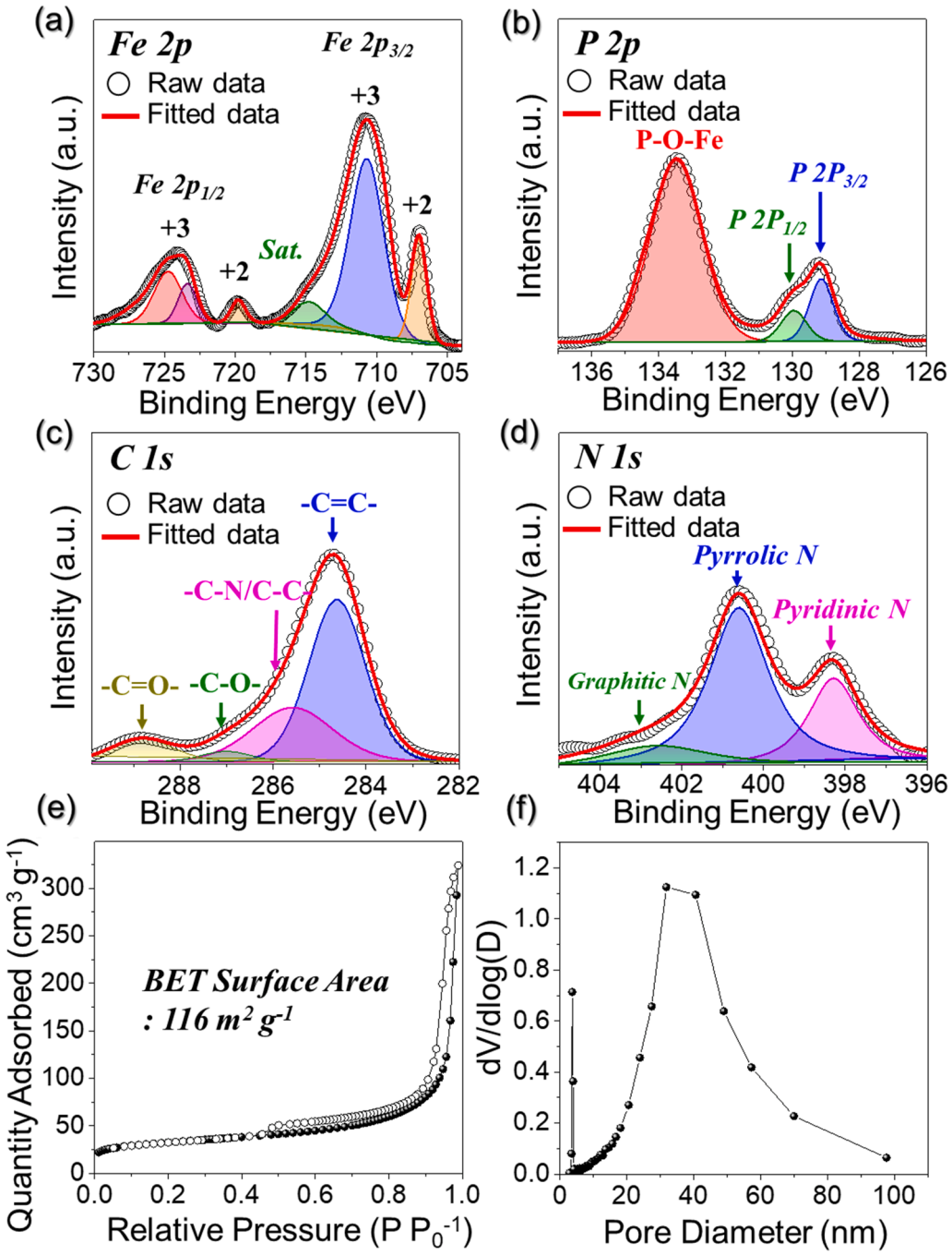

Fig. 3. (a) deconvoluted Fe 2p XPS spectrum, (b) deconvoluted P 2p XPS spectrum, (c) deconvoluted C 1 s XPS spectrum, (d) deconvoluted N 1 s XPS spectrum, (e) N_2 adsorption–desorption isotherm, and (f) BJH pore size distribution curve.

(P—O—Fe) when exposed to air [61,71]. The second predominant peak was deconvoluted using two closely spaced peaks, which were ascribed to the P $2p_{3/2}$ (129.1 eV) and P $2p_{1/2}$ (129.9 eV) orbitals [72]. The deconvoluted C 1 s XPS spectrum in Fig. 3c shows four well-fitted peaks centered at 284.6, 285.5, 287.0, and 288.8 eV related to the —C═C—, —C—N/C—C—, —C—O—, and —C═O— bonds, respectively [73]. The intense —C═C— peak strongly implied the presence of a carbon skeleton in the prepared nanostructure. Moreover, the existence of —C—N/C—C— confirms the presence of N-doped carbon, which is favorable for enhancing the overall electronic conductivity of nanostructure owing to the higher electronegative nature of the N than that of the C [64]. A well resolved N 1 s XPS spectrum was obtained (Fig. 3d), which confirms the existence of three well-fitted peaks at the binding energies of 398.2, 400.6, and 402.6 eV that are assigned to the pyridinic N, pyrrolic N, and graphitic N species, respectively [74]. The N content was further estimated to be 2.8 wt% using elemental analysis (Table S1) and was mainly induced by the *N*-rich organic groups present in the carbon precursor i.e., PVP. In addition, the estimated carbon content of ~ 11 wt% is consistent with the C 1 s XPS results displayed in Fig. 3c. These results verify the presence of the NGC framework in the prepared microspheres. Furthermore, the surface area of the P-Fe_xP@NGC microspheres was evaluated using adsorption–desorption curves by employing N_2 as an adsorbate gas (Fig. 3e). A high surface area of 116 m^2/g was attained mainly due to the existence of ordered arrays of the mesopores present all over the microsphere surface. The corresponding pore size distribution showing ordered mesopores (2–50 nm) with a peak maximum at ~

32 nm (Fig. 3f). Additionally, the sharp peak at 3.8 nm was attributed to the tensile effect of N_2 desorption [74]. The mesopores not only facilitate the efficient electrolyte percolation but also ensures sufficient space to accommodate the undesired volume perturbations during the redox processes.

To evaluate the structural advantages of the P-Fe$_x$P@NGC microspheres, a control sample (P-NGC) was prepared using the reduced powder after the intermediate heating step. The reduced powder was soaked in an acidic medium (HCl) for 3 days to remove metallic Fe and washed thoroughly with distilled water. Morphological and phase analyses of the control P-NGC samples are presented in Fig. 4. FE-SEM micrograph in Fig. 4a indicates that the spherical morphology was maintained even after prolonged acid etching. The FE-SEM images at high magnification (Fig. 4b and c) show the absence of Fe nanocrystals on the surface of the microspheres (compared with Fig. S2c), suggesting that the acid treatment successfully etched the metallic Fe. In addition, a highly ordered array of mesopores with an average diameter of 40 nm was also present, indicating that the porous structure of the microspheres was maintained. The TEM images shown in Fig. 4d also confirm the FE-SEM results with the presence of spherical-shaped microspheres (average diameter = 0.9 μm). The high magnification TEM image in Fig. 4e and f indicates the presence of uniformly present mesopores

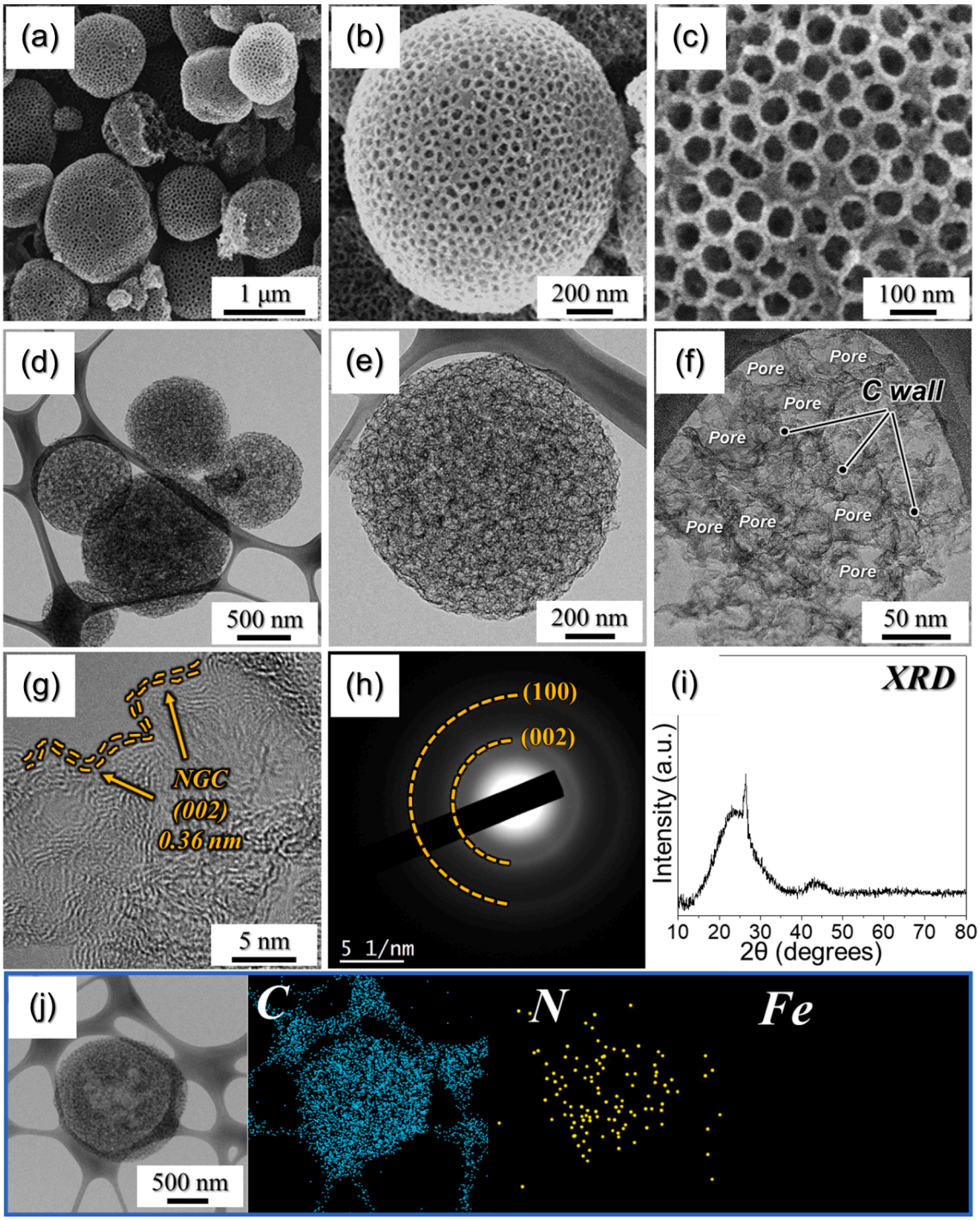

Fig. 4. Characterizations of the P-NGC microspheres obtained after the acid-etching process of reduced powder: (a,b) FE-SEM images, (c) high magnification FE-SEM image, (d-f) TEM images, (g) HR-TEM image, (h) SAED pattern, (i) XRD pattern, and (j) elemental mapping images.

(bright spots) within the carbon skeleton (grey region). Besides, no metallic Fe-nanocrystals were observed in the carbon framework. The corresponding HR-TEM image in Fig. 4g and SAED pattern in Fig. 4h also suggest the presence of the NGC framework only as highlighted by the *d*-spacing of 0.36 nm that corresponds to the (0 0 2) diffraction plane of graphitic carbon. Moreover, the XRD profile in Fig. 4i shows broad diffraction peaks at $2\theta = 24.3^{\circ}$ and 43.7°, which corresponds to the (0 0 2) and (1 0 0) diffraction planes of graphitic carbon, respectively. In addition, no diffraction peaks related to metallic Fe were observed, implying its complete removal. The elemental mapping results in Fig. 4j also confirm the presence of C and N only, indicating the formation of an N-doped carbonaceous framework without metallic Fe. Furthermore, the nitrogen content of 1.5 wt% in the P-NGC microspheres was quantified using elemental analysis (Table S1), confirming the successful *N*-doping of the carbonaceous framework. The Raman spectrum of the P-NGC microspheres (Fig. S3b) shows an I_D/IG ratio of ~ 0.93, suggesting the presence of graphitic carbon. Furthermore, the high surface area of 1142 m^2/g for P-NGC microspheres (Fig. S6a) firmly indicates that the metallic Fe nanocrystals were successfully removed from the microspheres, which is well synchronized with the results presented in Fig. 4e and f. The BJH pore size distribution (Fig. S6b) further reveals the existence of mesopores (average diameter of 40 nm). Overall, the above results confirm the effective removal of the metallic Fe using the acid treatment and the formation of highly porous NGC microspheres with an ordered array of mesopores.

3.2. Electrochemical performance

To validate the structural superiority of P-Fe$_x$P@NGC, its electrochemical performance was extensively investigated using the prepared microsphere powders. The prepared active materials were coated onto a Celgard separator as a multifunctional interlayer. Fig. S7 compares the

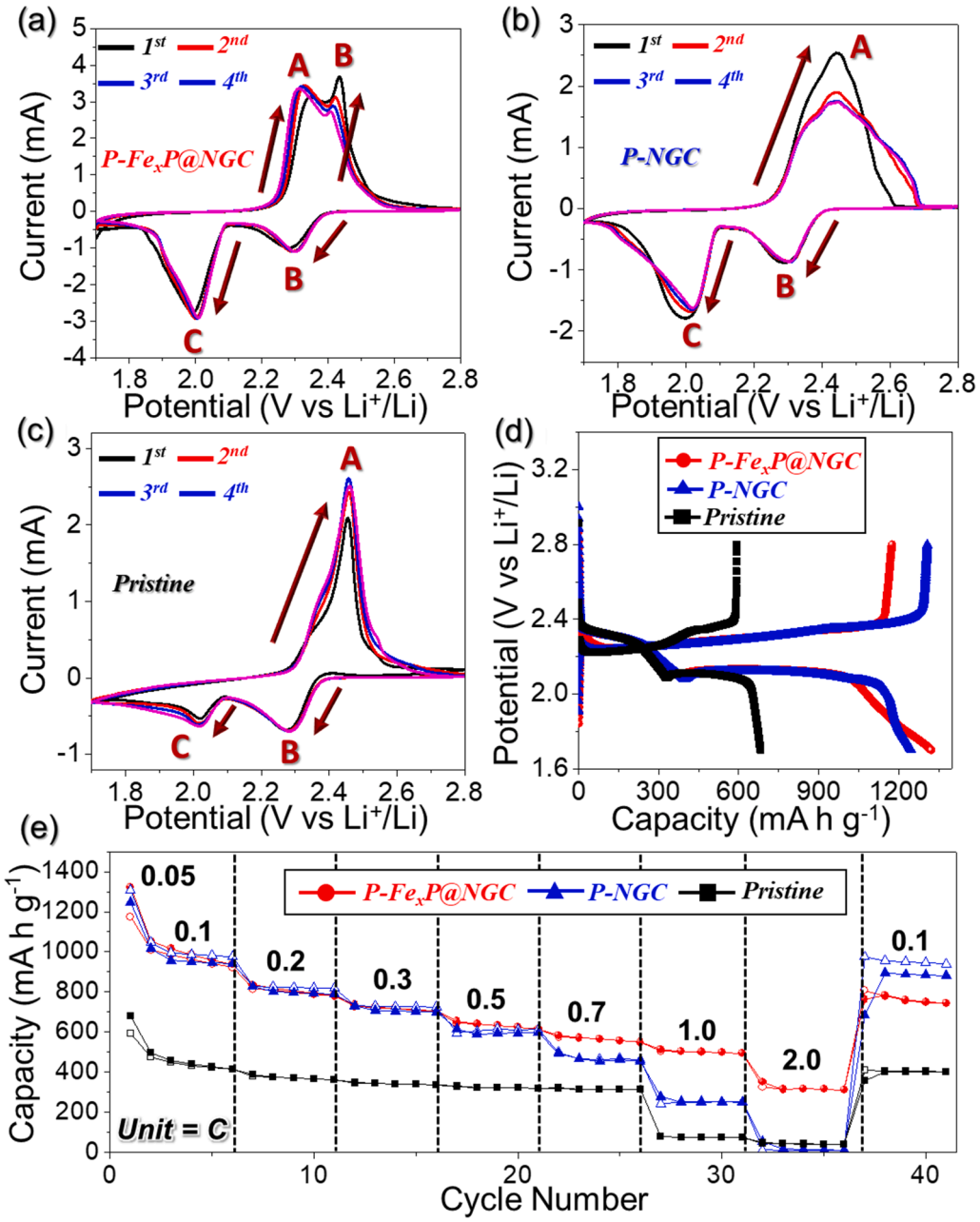

Fig. 5. Electrochemical performance of the Li–S cells with different separators: (a-c) cyclic voltammograms (CV) curves at 0.05 mV s^{-1} for four initial cycles, (d) initial charge–discharge profiles of the cells at 0.05C, and (e) rate-performance.

microstructural properties of the coated separator with the pristine separator. The FE-SEM micrograph of the pristine separator (inset in Fig. S7a) shows nanosized openings for facile diffusion of Li-ions. In contrast, the FE-SEM image of the separator coated with P-Fe$_x$P@NGC microspheres (inset in Fig. S7b) exhibits a homogeneous coating of 3-DOM microspheres and super-P. The coating thickness was *ca.* 10 μm (Fig. S7c). The CV curves of Li–S cells recorded with different coated separator arrangements are presented in Fig. 5. In the first CV scan, the P-Fe$_x$P@NGC microspheres-coated separator (Fig. 5a) exhibits well-distinguished and sharp reduction peaks at 2.28 and 1.99 V followed by closely spaced oxidation peaks at 2.34 and 2.43 V. The peaks at 2.28 and 1.99 V signify the reduction of elemental S to highly soluble high-order LiPSs (Li_2S_x; $6 \leq x \leq 8$) to middle-order polysulfides and then to insoluble low-order polysulfide (Li_2S_x; $x = 1$). During oxidation, a reverse mechanism occurred, i.e., oxidation of low-order polysulfide to high-order polysulfides (2.34 V) and then to elemental S (2.43 V). Similar CV curves were obtained for the cells employing the P-NGC microsphere-coated separator (Fig. 5b) and the pristine separator (Fig. 5c). However, among all tested cells, the cell employing the P-Fe$_x$P@NGC microsphere-coated separator showed the highest current intensity values, indicating enhanced redox kinetics inside the cell. To further confirm the CV results, initial voltage profiles were obtained at 0.05C (Fig. 5d). The Li–S cells utilizing the P-Fe$_x$P@NGC and P-NGC microsphere-coated separators showed typical charge–discharge voltage plateaus, suggesting that the redox reactions occur between elemental S and Li_2S. In addition, the charge–discharge voltage plateau positions were in line with those of CV curves. On the other hand, Li–S cell containing a pristine separator exhibited an orthodox voltage profile. Consequently, the cells employing P-Fe$_x$P@NGC, P-NGC, and pristine separators achieved discharge capacities of 1322, 1246, and 681 mA h g^{-1}, respectively. The high discharge capacity of Li–S cell featuring the P-Fe$_x$P@NGC-coated separator is attributed to the long voltage plateau that is due to the enhanced redox kinetics inside the cell, as indicated by the CV results. Overall, these kinetically favored redox processes can be ascribed to the highly porous nanostructure (ordered array of mesopores), conductive framework (NGC), and polar material (Fe$_x$P nanoparticles) present in P-Fe$_x$P@NGC microspheres. Moreover, these structural merits guarantee efficient electrolyte infiltration, fast charge transfer, and effective catalytic conversion of polysulfides that envisage enhanced electrochemical performance.

The Li–S cells employing different separators were further analyzed using rate capability tests in the range of 0.05–2.0C (Fig. 5e). The Li–S cell featuring the P-Fe$_x$P@NGC microspheres-coated separator achieved initial discharge capacities of 1322, 1053, 836, 736, 654, 583, 512, and 350 mA h g^{-1} at 0.05, 0.1, 0.2, 0.3, 0.5, 0.7, 1.0, and 2.0C-rate, respectively. In comparison, Li–S cell featuring P-NGC microspheres-

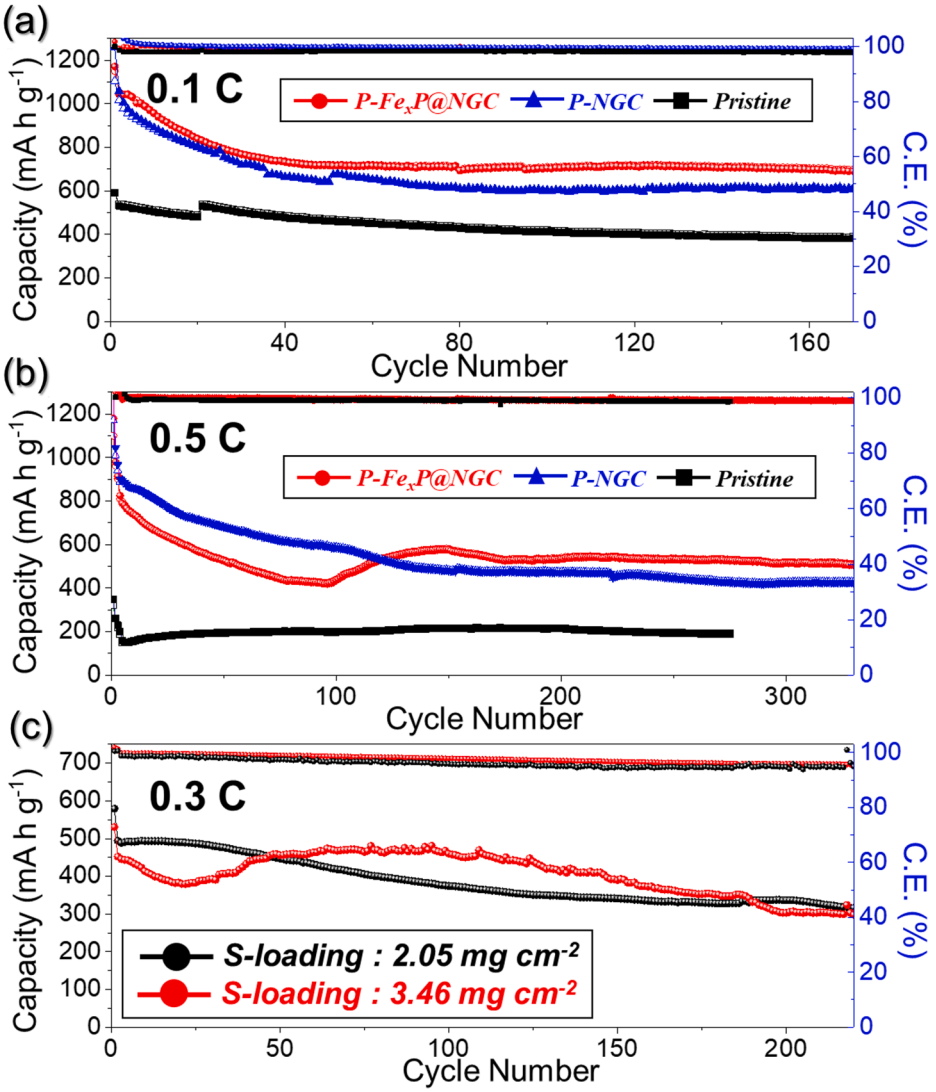

Fig. 6. Cycling performance of the Li-S cells with different separators at various C-rates: (a) 0.1C, (b) 0.5C, and (c) high-loading cycling performance for P-Fe$_x$P@NGC microspheres coated separator at 0.3C.

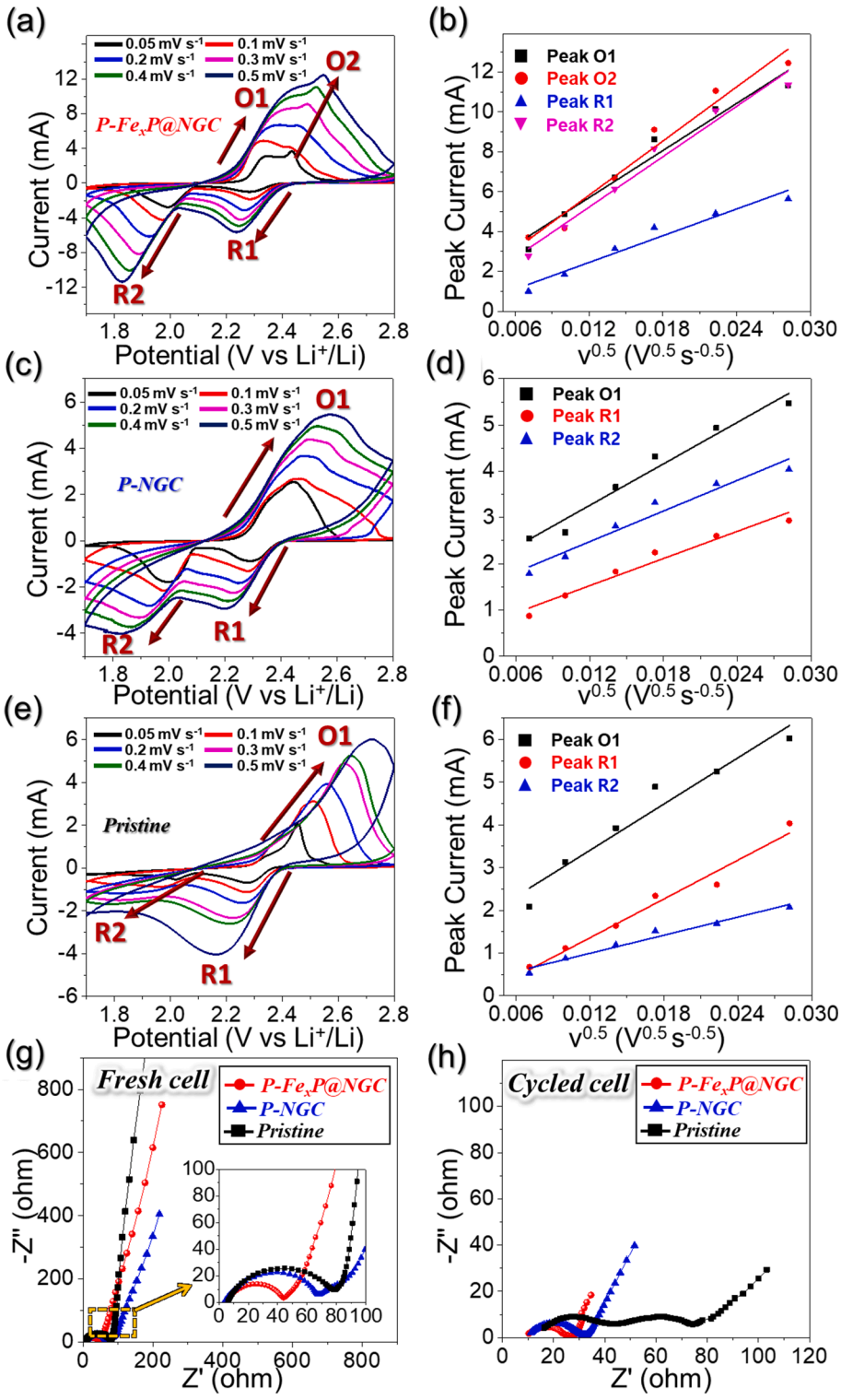

Fig. 7. Lithium-ion diffusion coefficient (D_{Li}^{+}) and Electrochemical impedance spectroscopy (EIS) spectra for the assembled Li–S cells with different separators: (a,c,e) Cyclic voltammograms at different scan rates ranging from 0.05 to 0.5 mV s^{-1}, (b,d,f) peak current vs square root of the voltage scan rate plots to calculate the D_{Li}^{+}; (g) EIS spectra of fresh cell, and (h) after 300th cycle at 0.5C-rate.

coated separator exhibited initial discharge capacities of 1247, 1016, 827, 731, 616, 492, 278, and 54 mA h g^{-1} at identical current rates. The similar discharge capacities in both cells, especially at low C-rates, were owing to the high surface area of P-NGC microspheres. However, due to the absence of the polar component (Fe_xP nanoparticles) in the P-NGC coating that could chemically anchor sulfur species, polysulfides diffused toward the Li-anode, that resulted in high active material loss and low discharge capacity values at high C-rates. Furthermore, when the C-rate was switched back to 0.1C, the P-Fe_xP@NGC microsphere-coated separator recovered slightly low discharge capacity compared to the P-NGC, primarily due to the high surface area of the later. However, a close examination clearly reveals a higher charge capacity than the discharge for the cell utilizing P-NGC interlayer, indicating insufficient LiPSs suppression compared to the P-Fe_xP@NGC cell. This implies

high reversibility of the redox processes with high Coulombic efficiency for P-Fe$_x$P@NGC-coated separator cell than the P-NGC cell. The high discharge capacities of the cell employing the P-Fe$_x$P@NGC microsphere-coated separator, even at high C-rates, indicate an efficient trapping and electrocatalytic conversion of the trapped polysulfides. In addition, the highly conductive NGC layer guarantees a rapid electron transfer during the redox process. This eventually resulted in high active material utilization (21 % at 2.0C). The charge–discharge voltage profiles of P-Fe$_x$P@NGC (Fig. S8a), and P-NGC (Fig. S8b) microsphere-coated separators at different C-rates firmly confirm this hypothesis. Furthermore, the cell employing the pristine separator (Fig. 5e) exhibited low discharge capacity values of 681, 496, 387, 350, 331, 322, 82, and 48 mA h g^{-1} at identical current rates, which was mainly owing to the high proportion of unutilized active substance. Overall, the rate capability tests proved the synergistic effect of highly porous, conductive, and polar nanostructures on the improved electrochemical performance.

The cycling performance of Li–S cells featuring separators with different coatings were also evaluated at different C-rates of 0.1, 0.5, and 1.0C, as shown in Figs. 6 and S9. Fig. 6a indicates that the Li–S cell utilizing the separator coated with P-Fe$_x$P@NGC exhibited a discharge capacity of 1043 mA h g^{-1} (62 % of theoretic value) during first cycle at 0.1C. The capacity decreases monotonically for a few tens of initial cycles, primarily because of the redistribution of sulfur species inside the cathode and stabilizes thereafter. After 170 cycles, the Li–S cell with the P-Fe$_x$P@NGC interlayer delivered a discharge capacity of 697 mA h g^{-1} (67 % capacity retention). In addition, the high Coulombic efficiency of 99.1 % at the end of 170th cycle indicated highly reversible electrochemical reactions inside the cell. Similarly, Li–S cells employing the separator coated with P-NGC exhibited a discharge capacity of 1057 mA h g^{-1} (63 % of theoretic value) during first cycle. However, the decrease in capacity was more pronounced during the few initial cycles. After 170 cycles, the Li–S cell with the P-NGC interlayer delivered a discharge capacity of 611 mA h g^{-1} (57 % capacity retention). In contrast, the pristine separator exhibited the lowest discharge capacity throughout the cycling process, mainly because of the absence of a conductive porous structure and polysulfide anchoring components. Similar cycling performances were observed for all Li–S cells tested at 0.5C-rate (Fig. 6b). Before that, the cells were charged–discharged for each cycle at 0.05, 0.1, 0.2, and 0.3C. Li–S cell with the P-Fe$_x$P@NGC interlayer showed a discharge capacity of 789 mA h g^{-1} (47 % of theoretic value), which decreased monotonically to 423 mA h g^{-1} after 98 cycles, primarily because of the redistribution of sulfur species in the cathodic region. Subsequently, the capacity increased to 575 mA h g^{-1} at the end of the 149th cycle because of the reactivation process of the trapped sulfur-like species and stabilized afterward. The cell exhibited a discharge capacity of 505 mA h g^{-1} (64 % capacity retention) after 330 continuous cycles with 0.11 % average capacity loss. The merits of employing P-Fe$_x$P@NGC interlayer were demonstrated by the extended cycling stability (Fig. S9a), in which a low-capacity loss of only 0.08 % per cycle occurred after 700 cycles at 0.5C-rate. In contrast, Li–S cell with the P-NGC interlayer demonstrated a higher discharge capacity of 891 mA h g^{-1} initially, mainly because of its ultra-high porous structure. However, the capacity continuously decreased owing to insufficient trapping and electrocatalytic conversion of polysulfide species, resulting in a lower discharge capacity of 425 mA h g^{-1} (47 % retention) after 330 cycles with an average capacity decay rate of 0.16 % per cycle. Similarly, the Li–S cell featuring the pristine separator showed poor cycling performance at low and high C-rates. Overall, the high-capacity retention and low capacity fading of the cell containing the P-Fe$_x$P@NGC-coated separator firmly verified the structural robustness and integrity. The highly porous nanostructure not only accommodates undesired volume changes but also offers efficient electrolyte infiltration inside the electrode, which allows facile and effective diffusion of charge species. Additionally, the highly conductive NGC framework offers numerous conductive paths for rapid electron transfer, thus encouraging kinetically favored redox reactions by lowering the charge-transfer resistance. The cycling stability of the Li–S cell featuring the P-Fe$_x$P@NGC-coated separator was also measured at a high C-rate of 1.0C, as shown in Fig. S9b. The cell exhibited an initial discharge capacity of 757 mA h g^{-1} (7th cycle), which stabilized at 321 mA h g^{-1} (42 % retention) after 300 cycles with an average capacity loss of 0.19 %, indicating high cycling stability. Further, the cycling stability was determined for Li–S cell featuring the P-Fe$_x$P@NGC-coated separator with high elemental S loadings and low electrolyte/sulfur (E/S) ratios (Fig. 6c). Consequently, initial discharge capacities (2nd cycle) of 494 and 452 mA h g^{-1} were achieved with an active material loading of 2.05 (E/S = 9.5 μL mg^{-1}) and 3.46 mg cm^{-2} (E/S = 5.6 μL mg^{-1}), respectively. The discharge capacity values after 220 continuous cycles were 316 and 298 mA h g^{-1}, indicating that even under extreme conditions, the structural advantages guarantee satisfactory electrochemical performance. Overall, the results obtained from the cycling performance tests confirmed that the novel structural design strategy played a major role in high active material utilization, sufficient electrode wetting, facile charge diffusion, faster redox processes, and efficient catalytic conversion of polysulfide species.

Further, the diffusion coefficient (D_{Li}^{+}) values were obtained to analyze the diffusion of Li-ions and redox kinetics inside the cells systematically. For this, CV curves of Li–S cells with P-Fe$_x$P@NGC-coated, P-NGC-coated, and pristine separators were acquired at various scan rates varying from 0.05 to 0.5 mV s^{-1}, as shown in Fig. 7a, c, and e. In the corresponding plots, the redox peak current was plotted against the square root of the scan rate to determine D_{Li}^{+}. The CV curves for the Li–S cell employing P-Fe$_x$P@NGC-, P-NGC-coated, and pristine separators show two pairs of reduction peaks (R1/R2) that can be ascribed to the reduction of elemental S to Li_2S *via* high- and intermediate-order polysulfides. During the oxidation process, the cell featuring the P-Fe$_x$P@NGC interlayer exhibited a two-step oxidation process (O1/O2) compared to the P-NGC-coated and pristine separators. Moreover, more symmetric CV curves with high current intensity values even at high scan rates of 0.5 mV s^{-1} were obtained for the cell with the P-Fe$_x$P@NGC interlayer, thus indicating enhanced redox reactions with faster Li-ion diffusion. To further validate this, the D_{Li}^{+} values were determined using the Randles–Sevick equation [13]:

$$I_p = 2.69 \times 10^5 \, n^{1.5} \, A \, D_{Li}^{+0.5} \, C_{Li} \, v^{0.5} \quad (1)$$

where *Ip* is redox current intensity, *n* is quantity of electrons participating in redox reactions, *A* is surface area of electrode (in cm^2), C_{Li} is concentration of Li-ions (in mol L^{-1}) whereas *v* represents scan rate (in V s^{-1}). The curves of the redox peak current (I_p) vs the square root of the voltage scan rate ($v^{0.5}$) and corresponding D_{Li}^{+} values for all tested Li–S cells are shown in Fig. 7b, d, and f, and Table S2, respectively. The Li–S cell featuring the P-Fe$_x$P@NGC-coated separator exhibited an order of magnitude higher D_{Li}^{+} value (10^{-7} cm^2 s^{-1}) than the Li–S cells utilizing the P-NGC-coated and pristine separators (10^{-8} cm^2 s^{-1}). The higher D_{Li}^{+} value firmly authenticates the structural merits of P-Fe$_x$P@NGC microspheres when employed as a multifunctional interlayer. The porous structure guarantees smooth diffusion of Li-ion which reduces the effective diffusion length. In addition, a highly conductive NGC framework facilitates rapid electron transfer during redox reactions by lowering the charge-transfer resistance in the electrode, thus enhancing the electrochemical performance.

To assess the surface kinetics at the electrode–separator–electrolyte interface, Nyquist plots were obtained using EIS for all assembled Li–S cells before (Fig. 7g) and after cycling (Fig. 7h). The impedance of the cells before cycling was measured at an open-circuit voltage while that of the cells after cycling was recorded in a fully charged state after 300 cycles at 0.5C-rate. The fitted parameters for all cells are encapsulated in Table S3. All tested Li–S cells exhibited small and similar solution resistance values (R_s) of 4–5 Ω, which implies a comparable electrolyte/electrode interface environment inside all cells. In addition, the cell

employing the separator coated with P-Fe$_x$P@NGC exhibited the lowest charge-transfer resistance (R_{ct}) of ~ 43 Ω than that of the cell employing the separator coated with P-NGC (72 Ω) and the pristine separator (~78 Ω), suggesting superior Li-ion diffusion. However, after 300 continuous redox cycles, the R_{ct} value for Li–S cells utilizing the P-Fe$_x$P@NGC- and P-NGC-coated separators decreased significantly to 17.5 and 23.2 Ω, respectively, compared to that of the pristine separator (66.8 Ω), thus implying superior surface kinetics. Besides, the Li-S cell featuring the pristine separator exhibits two semicircles in the EIS curve after cycling. The first semicircle in the high frequency is related to the formation of an insulating layer of the solid Li_2S_2/Li_2S between the separator and cathode [75]. In contrast, the introduction of P-Fe$_x$P@NGC and P-NGC microspheres as multifunctional interlayer suppress the LiPS diffusion, indicated by existence of only one semicicle. These results validate that the nanostructure advantages of P-Fe$_x$P@NGC offer excellent charge-transfer characteristics that not only reduce the cell resistance but also guarantee effective trapping and catalytic conversion of the polysulfide molecules along with better active material consumption even after extended cycling.

The catalytic properties of the as-prepared powders toward LiPS conversion were investigated using symmetric cells and visual tests. The CV curves of the assembled symmetric cells using the P-Fe$_x$P@NGC and P-NGC powders as counter and working electrodes are presented in Fig. 8a. The symmetrical cells containing P-Fe$_x$P@NGC electrodes exhibit sharp redox peaks supplemented with high current intensities, thus indicating efficient electrocatalytic conversion of polysulfide by the Fe$_x$P nanoparticles. The origin of the catalytic activity of the lithium polysulfides by the P-Fe$_x$P@NGC microspheres is primarily due to the formation of triple-phase boundaries between the catalyst (Fe$_x$P), conductive support (ordered mesoporous P-NGC microspheres), and electrolyte, which not only immobilize the sulfur species but also facilitate their electrocatalytic conversion, as reported previously [76]. In contrast, the CV curves of the cells employing P-NGC electrodes exhibit no redox peaks confirming the absence of the polysulfide catalytic conversion. Although the comparable current intensities for the P-NGC powders suggest the successful physical confinement of polysulfides, primarily due to the highly porous structure; however, the evidence for their catalytic conversion is missing. Similarly, the initial five CV curves of the symmetric cells employing P-Fe$_x$P@NGC (Fig. 8b) electrodes exhibit overlapping profiles, suggesting repeated catalytic conversion

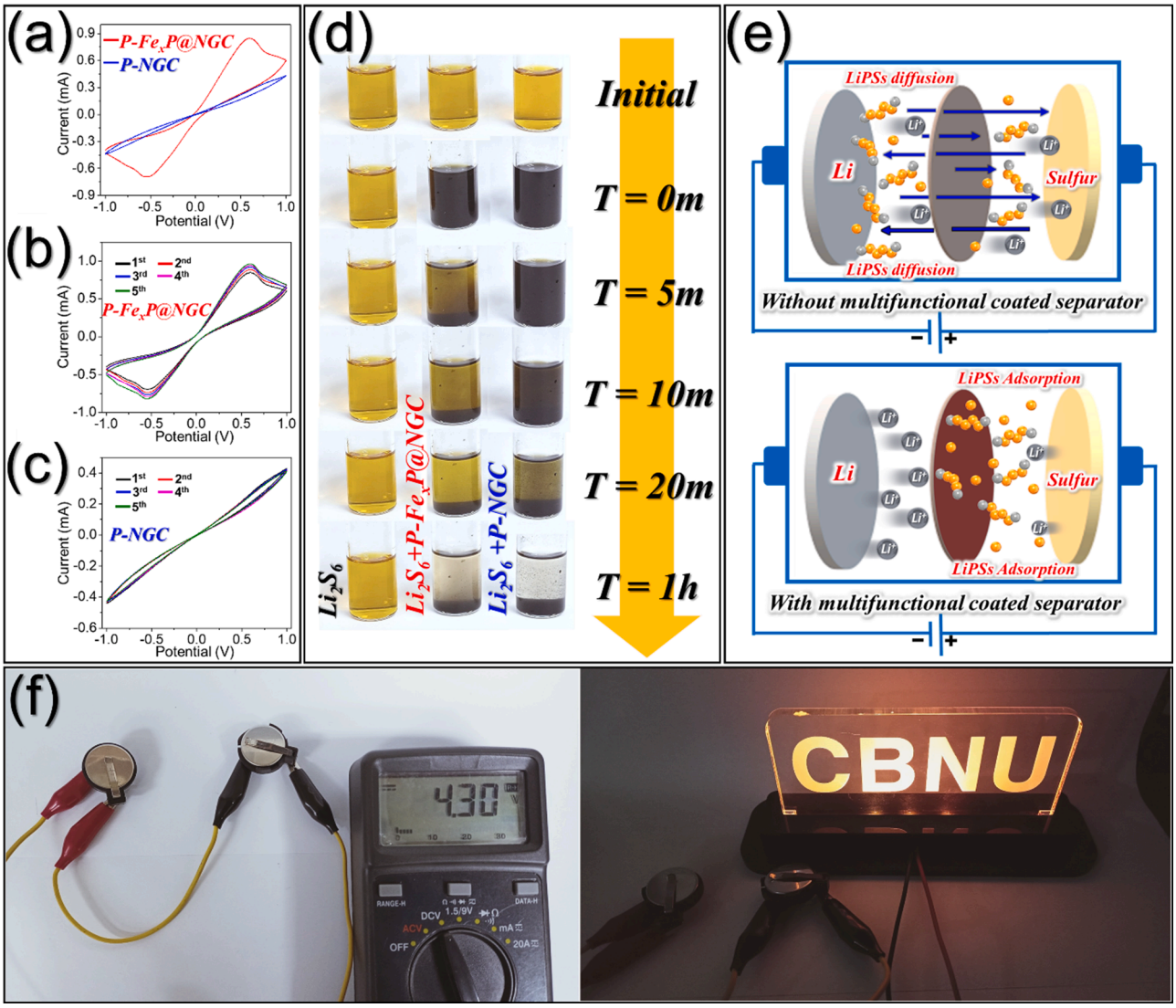

Fig. 8. Electrocatalytic activity and adsorption tests of lithium polysulfides using P-Fe$_x$P@NGC and P-NGC powders: (a) initial CV curves for different symmetric cells obtained at 3.0 mV s^{-1} in the voltage range of −1.0 to 1.0 V, (b) five initial CV cycles for symmetric cell employing P-Fe$_x$P@NGC microspheres, (c) five initial CV cycles for symmetric cell employing P-NGC microspheres, and (d) digital photographs of the lithium polysulfide adsorption test at different span of time, (e) schematic illustration of coated separator as multifunctional interlayer for trapping polysulfide species, and (f) digital photographs of a light-emitting diode (5 V, 10 mW) powered by series combination of two Li-S cells with sulfur loadings of 2.05 and 3.46 mg cm^{-2} after cycling at 0.3C-rate.

characteristics over cycling compared to the P-NGC (Fig. 8c). These results are supported by the visual polysulfide capturing tests presented in Fig. 8d. The color change from pale yellow (initial) to transparent (t = 1 h) upon the addition of the P-Fe$_x$P@NGC and P-NGC powders indicates strong polysulfide confinement characteristics of both powders. A schematic of the efficient trapping of polysulfides and other S species by the multifunctional P-Fe$_x$P@NGC microsphere-coated separator is presented in Fig. 8e. Additionally, to examine the applicability of the prepared multifunctional interlayers, Li–S cells featuring a P-Fe$_x$P@NGC microsphere-coated separator with high S loadings (2.05 and 3.46 mg cm^{-2}) were attached in series (Fig. 8f) with a load (light-emitting diode; 5 V, 10 mW). The digital photographs indicate that the Li–S batteries successfully powered the LED, thus envisaging the practical applicability of the prepared nanostructures as multifunctional interlayers.

The efficient adsorption and electrocatalytic conversion of polysulfide species were further validated using FE-SEM to analyze the morphologies of the separator coatings after cycling at 0.5C-rate (Fig. S10). The FE-SEM image presented in Fig. S10a indicates that the spherical morphology of P-Fe$_x$P@NGC coatings was retained even after prolonged cycling. Besides, the high-magnification FE-SEM image shown in Fig. S10b shows no polysulfide deposits, indicating the efficient catalytic conversion of trapped polysulfide species to elemental S by Fe$_x$P nanoparticles. This resulted in high sulfur utilization and enhanced electrochemical performance. In contrast, the FE-SEM micrographs of the P-NGC coating in Fig. S10c and d indicate large polysulfide deposits, primarily due to the nonpolar nature of the carbon that constitutes the microspheres. This leads to a high proportion of unutilized sulfur, and hence, inferior electrochemical properties. Lastly, the introduction of porous and conductive P-Fe$_x$P@NGC microspheres as a functional interlayer enhanced the electrochemical properties of Li–S batteries. Our design strategy resulted in efficient electrolyte percolation along with better diffusion of charged species, low volume changes, fast redox reaction kinetics, and effective anchoring of the polysulfide species.

4. Conclusions

In summary, we proposed a novel multifunctional interlayer for stable Li–S batteries which comprising three-dimensionally ordered mesoporous microspheres and well-embedded biphasic iron phosphide (Fe$_x$P) nanoparticles inside the N-doped graphitic carbon skeleton (P-Fe$_x$P@NGC). The highly porous structure not only guaranteed an efficient electrolyte infiltration but also shortened the effective diffusion length for charged species while channelizing the volume changes. Similarly, the highly conductive NGC framework not only enhanced the overall conductivity of the nanostructure but also offered numerous conductive channels for fast electron transfer, which eventually supported kinetically favored redox reactions. The polar Fe$_x$P nanoparticles acted as chemisorption active sites for the efficient chemical confinement and electrocatalytic conversion of polysulfide and other S-like species. Advancing from the structural benefits, Li–S cells featuring the P-Fe$_x$P@NGC-coated separator as functional interlayer demonstrated good rate performance (till 2.0C) and cycling stability at 0.1, 0.5, and 1.0C-rate. The enhanced electrochemical performance was credited to the facile diffusion of charged species, fast charge transfer, and efficient anchoring of polysulfide species, resulting in improved active material consumption. Therefore, we anticipate that the novel approach discussed here will provide significant understandings into the development of numerous conductive and porous nanostructures for wide applications.

Author contribution

Rakesh Saroha and Hye Seon ka designed the idea, performed all experiments, and prepare the initial blueprint of the manuscript. Jung Sang Cho supervise the work along with writing-review and editing. All authors discussed the results and provided valuable suggestions.

Declaration of Competing Interest

The authors declare that they have no known competing financial interests or personal relationships that could have appeared to influence the work reported in this paper.

Data availability

No data was used for the research described in the article.

Acknowledgments

This work was supported by the National Research Foundation of Korea (NRF) grant funded by the Korean government (MSIP) (No. NRF-2021R1A4A2001687, and NRF-2021R1I1A3057700. This work was partly supported by Korea Institute of Energy Technology Evaluation and Planning (KETEP) grant funded by the Korea government (MOTIE) (20224000000070, Human Resource Training for Smart Energy New Industry Cluster).

Appendix A. Supplementary data

Supplementary data to this article can be found online at https://doi.org/10.1016/j.apsusc.2022.155892.

References

[1] R. Saroha, A.K. Panwar, Y. Sharma, P.K. Tyagi, S. Ghosh, Development of surface functionalized ZnO-doped $LiFePO_4$/C composites as alternative cathode material for lithium ion batteries, Appl. Surf. Sci. 394 (2017) 25–36, https://doi.org/10.1016/j.apsusc.2016.09.105.

[2] R. Saroha, A.K. Panwar, Y. Sharma, Physicochemical and electrochemical performance of $LiFe_{1-x}Ni_xPO_4$ ($0 \leq x \leq 1.0$) solid solution as potential cathode material for rechargeable lithium-ion battery, Ceram. Int. 43 (2017) 5734–5742, https://doi.org/10.1016/j.ceramint.2017.01.115.

[3] R. Saroha, A. Gupta, A.K. Panwar, Electrochemical performances of Li-rich layered-layered Li_2MnO_3-$LiMnO_2$ solid solutions as cathode material for lithium-ion batteries, J. Alloys Compd. 696 (2017) 580–589, https://doi.org/10.1016/j.jallcom.2016.11.199.

[4] R. Saroha, J. Heo, X. Li, N. Angulakshmi, Y. Lee, H.-J. Ahn, J.-H. Ahn, J.-H. Kim, Asymmetric separator integrated with ferroelectric-$BaTiO_3$ and mesoporous-CNT for the reutilization of soluble polysulfide in lithium-sulfur batteries, J. Alloys Compd. 893 (2022), 162272, https://doi.org/10.1016/j.jallcom.2021.162272.

[5] R. Saroha, J.S. Cho, Nanofibers comprising interconnected chain-like hollow N-doped C nanocages as 3D free-standing cathodes for Li–S batteries with super-high sulfur content and lean electrolyte/sulfur ratio, Small Methods. 6 (5) (2022), https://doi.org/10.1002/smtd.202200049.

[6] W. Xue, L. Miao, L. Qie, C. Wang, S. Li, J. Wang, J. Li, Gravimetric and volumetric energy densities of lithium-sulfur batteries, Curr. Opin. Electrochem. 6 (2017) 92–99, https://doi.org/10.1016/j.coelec.2017.10.007.

[7] R. Saroha, J.-H. Ahn, J.S. Cho, A short review on dissolved lithium polysulfide catholytes for advanced lithium-sulfur batteries, Korean J. Chem. Eng. 38 (2021) 461–474, https://doi.org/10.1007/s11814-020-0729-5.

[8] R. Saroha, Y.H. Seon, B. Jin, Y.C. Kang, D.-W. Kang, S.M. Jeong, J.S. Cho, Self-supported hierarchically porous 3D carbon nanofiber network comprising Ni/Co/$NiCo_2O_4$ nanocrystals and hollow N-doped C nanocages as sulfur host for highly reversible Li–S batteries, Chem. Eng. J. 446 (2022), 137141, https://doi.org/10.1016/j.cej.2022.137141.

[9] H. Park, D.J. Siegel, Tuning the adsorption of polysulfides in lithium–sulfur batteries with metal–organic frameworks, Chem. Mater. 29 (2017) 4932–4939, https://doi.org/10.1021/acs.chemmater.7b01166.

[10] R. Saroha, J. Heo, Y. Liu, N. Angulakshmi, Y. Lee, K.-K. Cho, H.-J. Ahn, J.-H. Ahn, V_2O_3-decorated carbon nanofibers as a robust interlayer for long-lived, high-performance, room-temperature sodium–sulfur batteries, Chem. Eng. J. 431 (2022), 134205, https://doi.org/10.1016/j.cej.2021.134205.

[11] R. Saroha, J.H. Oh, Y.H. Seon, Y.C. Kang, J.S. Lee, D.W. Jeong, J.S. Cho, Freestanding interlayers for Li-S batteries: design and synthesis of hierarchically porous N-doped C nanofibers comprising vanadium nitride quantum dots and MOF-derived hollow N-doped C nanocages, J. Mater. Chem. A. 9 (2021) 11651–11664, https://doi.org/10.1039/D1TA01802G.

[12] C. Zu, Y. Fu, A. Manthiram, Highly reversible Li/dissolved polysulfide batteries with binder-free carbon nanofiber electrodes, J. Mater. Chem. A. 1 (2013) 10362–10367, https://doi.org/10.1039/c3ta11958k.

[13] R. Saroha, J.H. Oh, J.S. Lee, Y.C. Kang, S.M. Jeong, D.-W. Kang, C. Cho, J.S. Cho, Hierarchically porous nanofibers comprising multiple core–shell Co_3O_4@graphitic

carbon nanoparticles grafted within N-doped CNTs as functional interlayers for excellent Li–S batteries, Chem. Eng. J. 426 (2021), 130805, https://doi.org/10.1016/j.cej.2021.130805.
[14] D. Wang, Q. Cao, B. Jing, X. Wang, T. Huang, P. Zeng, S. Jiang, Q. Zhang, J. Sun, A freestanding metallic tin-modified and nitrogen-doped carbon skeleton as interlayer for lithium-sulfur battery, Chem. Eng. J. 399 (2020), 125723, https://doi.org/10.1016/j.cej.2020.125723.
[15] Y.H. Seon, R. Saroha, J.S. Cho, Hierarchically porous N-doped C nanofibers comprising TiO_2 quantum dots and ZIF-8-derived hollow C nanocages as ultralight interlayer for stable Li–S batteries, Compos. B Eng. 237 (2022), 109856, https://doi.org/10.1016/j.compositesb.2022.109856.
[16] X.-Y. Li, S. Feng, C.-X. Zhao, Q. Cheng, Z.-X. Chen, S.-Y. Sun, X. Chen, X.-Q. Zhang, B.-Q. Li, J.-Q. Huang, Q. Zhang, Regulating lithium salt to inhibit surface gelation on an electrocatalyst for high-energy-density lithium-sulfur batteries, J. Am. Chem. Soc. 144 (2022) 14638–14646, https://doi.org/10.1021/jacs.2c04176.
[17] Z. Shen, X. Jin, J. Tian, M. Li, Y. Yuan, S. Zhang, S. Fang, X. Fan, W. Xu, H. Lu, J. Lu, H. Zhang, Cation-doped ZnS catalyst for polysulfide conversion in lithium-sulfur batteries, Nat. Catal. 5 (2022) 555–563, https://doi.org/10.1038/s41929-022-00804-4.
[18] X.-Y. Li, S. Feng, M. Zhao, C.-X. Zhao, X. Chen, B.-Q. Li, J.-Q. Huang, Q. Zhang, Surface gelation on disulfide electrocatalyst for lithium-sulfur batteries, Angew. Chem. Int. Ed. 61 (2022) e202114671.
[19] Y.-W. Song, J.-L. Qin, C.-X. Zhao, M. Zhao, L.-P. Hou, Y.-Q. Peng, H.-J. Peng, B.-Q. Li, The formation of crystalline lithium sulfide on electrocatalytic surfaces in lithium-sulfur batteries, J. Energy Chem. 64 (2022) 678–1573, https://doi.org/10.1016/j.jechem.2021.05.023.
[20] C.-X. Zhao, X.-Y. Li, M. Zhao, Z.-X. Chen, Y.-W. Song, W.-J. Chen, J.-N. Liu, B. Wang, X.-Q. Zhang, C.-M. Chen, B.-Q. Li, J.-Q. Huang, Q. Zhang, Semi-immobilized molecular electrocatalysts for high-performance lithium-sulfur batteries, J. Am. Chem. Soc. 143 (2021) 19865–19872, https://doi.org/10.1021/jacs.1c09107.
[21] M. Yang, D. Shi, X. Sun, Y. Li, Z. Liang, L. Zhang, Y. Shao, Y. Wu, X. Hao, Shuttle confinement of lithium polysulfides in borocarbonitride nanotubes with enhanced performance for lithium–sulfur batteries, J. Mater. Chem. A. 8 (2020) 296–304, https://doi.org/10.1039/C9TA11500E.
[22] D.-W. Wang, Q. Zeng, G. Zhou, L. Yin, F. Li, H.-M. Cheng, I.R. Gentle, G.Q.M. Lu, Carbon–sulfur composites for Li–S batteries: status and prospects, J. Mater. Chem. A. 1 (2013) 9382–9394, https://doi.org/10.1039/c3ta11045a.
[23] Z. Li, Y. Huang, L. Yuan, Z. Hao, Y. Huang, Status and prospects in sulfur–carbon composites as cathode materials for rechargeable lithium–sulfur batteries, Carbon 92 (2015) 41–63, https://doi.org/10.1016/j.carbon.2015.03.008.
[24] M. Sevilla, J. Carro-Rodríguez, N. Díez, A.B. Fuertes, Straightforward synthesis of sulfur/N, S-codoped carbon cathodes for lithium-sulfur batteries, Sci. Rep. 10 (2020) 4866, https://doi.org/10.1038/s41598-020-61583-1.
[25] P. Chiochan, S. Kaewruang, N. Phattharasupakun, J. Wutthiprom, T. Maihom, J. Limtrakul, S.S. Nagarkar, S. Horike, M. Sawangphruk, Chemical adsorption and physical confinement of polysulfides with the Janus-faced interlayer for high-performance lithium-sulfur batteries, Sci. Rep. 7 (2017) 17703, https://doi.org/10.1038/s41598-017-18108-0.
[26] N. Deng, E.B. Ticha, L. Wang, Q. Li, H. Zhao, L. Gao, M. Liu, Y. Liu, W. Kang, B. Cheng, Physical inhibition and chemical confinement of lithium polysulfides by designing a double-layer composite separator for lithium-sulfur battery, ChemElectroChem 6 (2019) 4817–4830, https://doi.org/10.1002/celc.201901131.
[27] T. Tang, Y. Hou, Chemical confinement and utility of lithium polysulfides in lithium sulfur batteries, Small Methods. 4 (2020) 1900001, https://doi.org/10.1002/smtd.201900001.
[28] Y. Wang, Y. Meng, Z. Zhang, Y. Guo, D. Xiao, Trifunctional electrolyte additive Hexadecyltrioctylammonium iodide for lithium–sulfur batteries with extended cycle life, ACS Appl. Mater. Interfaces. 13 (2021) 16545–16557, https://doi.org/10.1021/acsami.1c02580.
[29] A. Singh, A. Rafie, V. Kalra, Revisiting the use of electrolyte additives in Li–S batteries: the role of porosity of sulfur host materials, Sustain. Energy Fuels. 3 (2019) 2788–2797, https://doi.org/10.1039/C9SE00277D.
[30] H.-L. Wu, M. Shin, Y.-M. Liu, K.A. See, A.A. Gewirth, Thiol-based electrolyte additives for high-performance lithium-sulfur batteries, Nano Energy 32 (2017) 50–58, https://doi.org/10.1016/j.nanoen.2016.12.015.
[31] C. Yan, X.-Q. Zhang, J.-Q. Huang, Q. Liu, Q. Zhang, Lithium-anode protection in lithium–sulfur batteries, J. Trends Chem. 1 (2019) 693–704, https://doi.org/10.1016/j.trechm.2019.06.007.
[32] Y.-X. Yao, X.-Q. Zhang, B.-Q. Li, C. Yan, P.-Y. Chen, J.-Q. Huang, Q. Zhang, A compact inorganic layer for robust anode protection in lithium-sulfur batteries, InfoMat. 2 (2) (2020) 379–388.
[33] X.-B. Cheng, J.-Q. Huang, Q. Zhang, Review—Li metal anode in working lithium-sulfur batteries, J. Electrochem. Soc. 165 (2018) A6058–A6072, https://doi.org/10.1149/2.0111801jes.
[34] B. Liu, V.S. Thoi, Tailored porous framework materials for advancing lithium–sulfur batteries, Chem. Commun. (Camb) 58 (2022) 4005–4015, https://doi.org/10.1039/d1cc07087h.
[35] R. Chulliyote, H. Hareendrakrishnakumar, M.G. Joseph, Hierarchical porous carbon material with multifunctionalities derived from honeycomb as a sulfur host and laminate on the cathode for high-performance lithium–sulfur batteries, ACS Sustainable Chem. Eng. 7 (2019) 19344–19355, https://doi.org/10.1021/acssuschemeng.9b02560.
[36] M. Wang, X. Xia, Y. Zhong, J. Wu, R. Xu, Z. Yao, D. Wang, W. Tang, X. Wang, J. Tu, Porous carbon hosts for lithium–sulfur batteries, Chemistry 25 (2019) 3710–3725, https://doi.org/10.1002/chem.201803153.
[37] T. Wang, Y. Liu, X. Liu, G. Cui, Y. Zhang, X. Wang, Three-dimensionally ordered macro-porous metal-organic framework for high-performance lithium-sulfur battery, ChemElectroChem 9 (2022) e202101099.
[38] R. Ryoo, S.H. Joo, S. Jun, Synthesis of highly ordered carbon molecular sieves via template-mediated structural transformation, J. Phys. Chem. B. 103 (1999) 7743–7746, https://doi.org/10.1021/jp991673a.
[39] J. Lee, S. Yoon, T. Hyeon, S.M. Oh, K.B. Kim, Synthesis of a new mesoporous carbon and its application to electrochemical double-layer capacitors, Chem. Commun. (21) (1999) 2177–2178.
[40] S. Jun, S.H. Joo, R. Ryoo, M. Kruk, M. Jaroniec, Z. Liu, T. Ohsuna, O. Terasaki, Synthesis of new, nanoporous carbon with hexagonally ordered mesostructure, J. Am. Chem. Soc. 122 (2000) 10712–10713, https://doi.org/10.1021/ja002261e.
[41] J. Schuster, G. He, B. Mandlmeier, T. Yim, K.T. Lee, T. Bein, L.F. Nazar, Spherical ordered mesoporous carbon nanoparticles with high porosity for lithium–sulfur batteries, Angew. Chem. 51 (2012) 3651–3655, https://doi.org/10.1002/anie.201107817.
[42] T.G. Jeong, J. Chun, B.W. Cho, J. Lee, Y.T. Kim, Enhanced performance of sulfur-infiltrated bimodal mesoporous carbon foam by chemical solution deposition as cathode materials for lithium sulfur batteries, Sci. Rep. 7 (2017) 42238, https://doi.org/10.1038/srep42238.
[43] S. Khan, M. Ul-Islam, M. Sajjad, I. Hussain, M. Idrees, M. Saeed, M. Imran, M. S. Javed, Nitrogen and sulfur co-doped two-dimensional highly porous carbon nanosheets for high-performance lithium–sulfur batteries, Energy Fuels. 36 (2022) 2220–2227, https://doi.org/10.1021/acs.energyfuels.1c04231.
[44] S. Li, X. Chen, F. Hu, R. Zeng, Y. Huang, L. Yuan, J. Xie, Cobalt-embedded carbon nanofiber as electrocatalyst for polysulfide redox reaction in lithium sulfur batteries, Electrochim. Acta. 304 (2019) 11–19, https://doi.org/10.1016/j.electacta.2019.02.087.
[45] W. Ren, L. Xu, L. Zhu, X. Wang, X. Ma, D. Wang, Cobalt-doped vanadium nitride yolk–shell nanospheres@carbon with physical and chemical synergistic effects for advanced Li–S batteries, ACS Appl. Mater. Interfaces. 10 (2018) 11642–11651, https://doi.org/10.1021/acsami.7b18955.
[46] C. Ye, Y. Jiao, H. Jin, A.D. Slattery, K. Davey, H. Wang, S.Z. Qiao, 2D MoN-VN heterostructure to regulate polysulfides for highly efficient lithium-sulfur batteries, Angew. Chem. Int. Ed. Engl. 57 (2018) 16703–16707, https://doi.org/10.1002/anie.201810579.
[47] S. Liu, Y. Li, C. Zhang, X. Chen, Z. Wang, F. Cui, X. Yang, W. Yue, Amorphous TiO_2 nanofilm interface coating on mesoporous carbon as efficient sulfur host for lithium–sulfur batteries, Electrochim. Acta. 332 (2020), 135458, https://doi.org/10.1016/j.electacta.2019.135458.
[48] L. Zhou, H. Li, X. Wu, Y. Zhang, D.L. Danilov, R.-A. Eichel, P.H.L. Notten, Double-shelled Co_3O_4/C nanocages enabling polysulfides adsorption for high-performance lithium–sulfur batteries, ACS Appl. Energy Mater. 2 (11) (2019) 8153–8162.
[49] G. Liang, J. Wu, X. Qin, M. Liu, Q. Li, Y.B. He, J.K. Kim, B. Li, F. Kang, Ultrafine TiO_2 decorated carbon nanofibers as multifunctional interlayer for high-performance lithium–sulfur battery, ACS Appl. Mater. Interfaces. 8 (2016) 23105–23113, https://doi.org/10.1021/acsami.6b07487.
[50] P. Guo, D. Liu, Z. Liu, X. Shang, Q. Liu, D. He, Dual functional MoS_2/graphene interlayer as an efficient polysulfide barrier for advanced lithium-sulfur batteries, Electrochim. Acta. 256 (2017) 28–36, https://doi.org/10.1016/j.electacta.2017.10.003.
[51] S. Jiang, M. Chen, X. Wang, P. Zeng, Y. Li, H. Liu, X. Li, C. Huang, H. Shu, Z. Luo, C. Wu, A tin disulfide nanosheet wrapped with interconnected carbon nanotube networks for application of lithium sulfur batteries, Electrochim. Acta. 313 (2019) 151–160, https://doi.org/10.1016/j.electacta.2019.05.001.
[52] J. Park, B.C. Yu, J.S. Park, J.W. Choi, C. Kim, Y.E. Sung, J.B. Goodenough, Tungsten disulfide catalysts supported on a carbon cloth interlayer for high performance Li–S battery, Adv. Energy Mater. 7 (2017) 1602567, https://doi.org/10.1002/aenm.201602567.
[53] W. Sun, Y. Li, S. Liu, C. Liu, X. Tan, K. Xie, Mechanism investigation of iron selenide as polysulfide mediator for long-life lithium-sulfur batteries, Chem. Eng. J. 416 (2021), 129166, https://doi.org/10.1016/j.cej.2021.129166.
[54] W. Xiao, Q. He, Y. Zhao, Virtual screening of two-dimensional selenides and transition metal doped SnSe for lithium-sulfur batteries: A first-principles study, Appl. Surf. Sci. 570 (2021), 151213, https://doi.org/10.1016/j.apsusc.2021.151213.
[55] Y. Tian, G. Li, Y. Zhang, D. Luo, X. Wang, Y. Zhao, H. Liu, P. Ji, X. Du, J. Li, Z. Chen, Low-bandgap Se-deficient antimony selenide as a multifunctional polysulfide barrier toward high-performance lithium–sulfur batteries, Adv. Mater. 32 (4) (2020) 1904876.
[56] T. Yim, S.H. Han, N.H. Park, M.S. Park, J.H. Lee, J. Shin, J.W. Choi, Y. Jung, Y. N. Jo, J.S. Yu, K.J. Kim, Effective polysulfide rejection by dipole-aligned $BaTiO_3$ coated separator in lithium–sulfur batteries, Adv. Funct. Mater. 26 (2016) 7817–7823, https://doi.org/10.1002/adfm.201602498.
[57] H. Li, L. Sun, Y. Zhao, T. Tan, Y. Zhang, A novel CuS/graphene-coated separator for suppressing the shuttle effect of lithium/sulfur batteries, Appl. Surf. Sci. 466 (2019) 309–319, https://doi.org/10.1016/j.apsusc.2018.10.046.
[58] J. Yao, M. Zhang, G. Han, X. Wang, Z. Wang, J. Wang, Reduced graphene oxide coated Fe-soc as a cathode material for high-performance lithium-sulfur batteries, Ceram. Int. 46 (2020) 24155–24161, https://doi.org/10.1016/j.ceramint.2020.06.195.
[59] F. Zhang, Z. Li, T. Cao, K. Qin, Q. Xu, H. Liu, Y. Xia, Multishelled Ni_2P microspheres as multifunctional sulfur host 3D-printed cathode materials ensuring high areal

capacity of Lithium-Sulfur batteries, ACS Sustain. Chem. Eng. 9 (2021) 6097–6106, https://doi.org/10.1021/acssuschemeng.1c01580.
[60] H. Yuan, X. Chen, G. Zhou, W. Zhang, J. Luo, H. Huang, Y. Gan, C. Liang, Y. Xia, J. Zhang, J. Wang, X. Tao, Efficient activation of Li_2S by transition metal phosphides nanoparticles for highly stable lithium–sulfur batteries, ACS Energy Lett. 2 (2017) 1711–1719, https://doi.org/10.1021/acsenergylett.7b00465.
[61] Y. Li, X. Lei, Y. Yuan, S. Wu, B. Han, X. Liu, W. Liu, J. Hu, C. Yang, Z. Lin, J. Lu, Fe_2P-decorated N, P codoped carbon synthesized via direct biological recycling for endurable sulfur encapsulation, ACS Cent. Sci. 6 (2020) 1827–1834, https://doi.org/10.1021/acscentsci.0c00899.
[62] M.S. Jo, S. Ghosh, S.M. Jeong, Y.C. Kang, J.S. Cho, Coral-like yolk–shell-structured nickel oxide/carbon composite microspheres for high-performance Li-ion storage anodes, Nano Micro Lett. 11 (2019) 3, https://doi.org/10.1007/s40820-018-0234-0.
[63] R. Saroha, A.K. Panwar, Effect of in situ pyrolysis of acetylene (C_2H_2) gas as a carbon source on the electrochemical performance of $LiFePO_4$ for rechargeable lithium-ion batteries, J. Phys. D: Appl. Phys. 50 (25) (2017) 255501.
[64] J.S. Lee, R. Saroha, J.S. Cho, Porous microspheres comprising $CoSe_2$ nanorods coated with N-doped graphitic C and polydopamine-derived C as anodes for long-lived Na-ion batteries, Nano Micro Lett. 14 (2022) 1–22, https://doi.org/10.1007/s40820-022-00855-z.
[65] J.S. Lee, R. Saroha, J.H. Oh, C. Cho, B. Jin, D.-W. Kang, J.S. Cho, Camphene-derived hollow and porous nanofibers decorated with hollow NiO nanospheres and graphitic carbon as anodes for efficient lithium-ion storage, J. Ind. Eng. Chem. 114 (2022) 276–287, https://doi.org/10.1016/j.jiec.2022.07.017.
[66] S.H. Oh, S.M. Park, D.-W. Kang, Y.C. Kang, J.S. Cho, Fibrous network of highly integrated carbon nanotubes/MoO_3 composite bundles anchored with MoO_3 nanoplates for superior lithium ion battery anodes, J. Ind. Eng. Chem. 83 (2020) 438–448, https://doi.org/10.1016/j.jiec.2019.12.017.
[67] H. Huang, C. Yu, J. Yang, X. Han, C. Zhao, S. Li, Z. Liu, J. Qiu, Ultrasmall diiron phosphide nanodots anchored on graphene sheets with enhanced electrocatalytic activity for hydrogen production via high-efficiency water splitting, J. Mater. Chem. A. 4 (2016) 16028–16035, https://doi.org/10.1039/C6TA05086G.
[68] L. Li, P. Ma, S. Hussain, L. Jia, D. Lin, X. Yin, Y. Lin, Z. Cheng, L. Wang, FeS_2/carbon hybrids on carbon cloth: a highly efficient and stable counter electrode for dye-sensitized solar cells, Sustain. Energy Fuels. 3 (2019) 1749–1756, https://doi.org/10.1039/C9SE00240E.
[69] Y. Xu, T. Feng, Z. Cui, P. Guo, W. Wang, Z. Li, Fe_7S_8/FeS_2/C as an efficient catalyst for electrocatalytic water splitting, Int. J. Hydrog. Energy. 46 (2021) 39216–39225, https://doi.org/10.1016/j.ijhydene.2021.09.159.
[70] W.H. Yun, G. Das, B. Kim, B.J. Park, H.H. Yoon, Y.S. Yoon, Ni-Fe phosphide deposited carbon felt as free-standing bifunctional catalyst electrode for urea electrolysis, Sci. Rep. 11 (2021) 22003, https://doi.org/10.1038/s41598-021-01383-3.
[71] M. Shimizu, Y. Tsushima, S. Arai, Electrochemical Na-insertion/extraction property of Ni-coated black phosphorus prepared by an electroless deposition method, ACS Omega 2 (2017) 4306–4315, https://doi.org/10.1021/acsomega.7b00950.
[72] X. Wu, K. Gong, G. Zhao, W. Lou, X. Wang, W. Liu, Mechanical synthesis of chemically bonded phosphorus–graphene hybrid as high-temperature lubricating oil additive, RSC Adv. 8 (2018) 4595–4603, https://doi.org/10.1039/c7ra11691h.
[73] J.S. Lee, M.S. Jo, R. Saroha, D.S. Jung, Y.H. Seon, J.S. Lee, Y.C. Kang, D.W. Kang, J. S. Cho, Hierarchically well-developed porous graphene nanofibers comprising N-doped graphitic C-coated cobalt oxide hollow nanospheres as anodes for high-rate Li-ion batteries, Small. 16 (2020) e2002213. https://doi.org/10.1002/smll.202002213.
[74] M.S. Jo, J.S. Lee, S.Y. Jeong, J.K. Kim, Y.C. Kang, D.W. Kang, S.M. Jeong, J.S. Cho, Golden bristlegrass-like hierarchical graphene nanofibers entangled with N-doped CNTs containing $CoSe_2$ nanocrystals at each node as anodes for high-rate sodium-ion batteries, Small 16 (38) (2020) 2003391.
[75] Z.A. Ghazi, X. He, A.M. Khattak, N.A. Khan, B. Liang, A. Iqbal, J. Wang, H. Sin, L. Li, Z. Tang, MoS_2/celgard separator as efficient polysulfide barrier for long-life lithium-sulfur batteries, Adv. Mater. 29 (2017) 1606817, https://doi.org/10.1002/adam.201606817.
[76] C. Zhao, G.-L. Xu, Z. Yu, L. Zhang, I. Hwang, Y.-X. Mo, Y. Ren, L. Cheng, C.-J. Sun, Y. Ren, X. Zuo, J.-T. Li, S.-G. Sun, K. Amine, T. Zhao, A high-energy and long cycling lithium-sulfur pouch cell via a macroporous catalytic cathode with double-end binding sites, Nat. Nanotechnol. 16 (2021) 166–173, https://doi.org/10.1038/s41565-020-00797.